The Astrophysical Journal, 1010:1 (29pp), 2026 October 10 https://doi.org/10.3847/1538-4357/ae88fe
© 2026. The Author(s). Published by the American Astronomical Society.
OPEN ACCESS

Extreme Debris Disks: Insights into Violent Collisions in Planet Formation and Destruction

Kate Y. L. Su[1], Attila Moór[2,3], Ágnes Kóspál[2,3], George H. Rieke[4,5], Antranik A. Sefilian[4], Renu Malhotra[5], Ilaria Pascucci[5], Alan P. Jackson[6], Péter Ábrahám[2,3,7], and Nicholas P. Ballering[1,8]
[1] Space Science Institute, 4750 Walnut Street, Suite 205, Boulder, CO 80301, USA; ksu@spacescience.org
[2] Konkoly Observatory, HUN-REN Research Centre for Astronomy and Earth Sciences, MTA Centre of Excellence, Konkoly-Thege Miklós út 15-17, 1121 Budapest, Hungary
[3] CSFK, MTA Centre of Excellence, Budapest, Konkoly Thege Miklós út 15-17., H-1121, Hungary
[4] Department of Astronomy and Steward Observatory, University of Arizona, Tucson, AZ 85721, USA
[5] Lunar and Planetary Laboratory, The University of Arizona, Tucson, AZ 85721, USA
[6] Department of Physics, Astronomy, and Geosciences, Towson University, 8000 York Road, Towson, MD, USA
[7] Department of Astrophysics, University of Vienna, Türkenschanzstr. 17, A-1180 Vienna, Austria
[8] Department of Astronomy, University of Wisconsin-Madison, Madison, WI 53706, USA
Received 2026 February 10; revised 2026 May 21; accepted 2026 July 2; published 2026 October 1

Abstract

Debris disks are dusty structures around mature stars, primarily identified by infrared excesses in the stellar spectra. A subset, known as extreme debris disks (EDDs), exhibits stochastic infrared variability, believed to result from large-scale violent collisions that contribute to the formation or destruction of rocky planetary bodies. We analyze JWST and Spitzer mid-infrared spectra for 21 EDDs to investigate the connection between impact-produced dust mineralogy and the age and dynamical state of these systems during various stages of planet formation and evolution. Our findings indicate that EDDs contain significantly more optically thin, small dust grains compared to those typically seen in protoplanetary and debris disks. Predominantly submicron in size, these grains are thermally altered, as shown by their high levels of silica and crystalline silicate composition. Along with stochastic infrared variability, these features define EDDs as a subclass of debris systems where dust is generated from large collisions between Moon- and Mars-sized bodies. Our results not only provide diagnostic information about the physical conditions of violent events during terrestrial planet formation, aiding in differentiating the complex outcomes of these impacts, but also offer a potential marker for identifying planetary systems experiencing dynamical instability.

Unified Astronomy Thesaurus concepts: Planetary system formation (1257); Planetary system evolution (2292); Circumstellar matter (241); Debris disks (363); Circumstellar dust (236); Circumstellar grains (239); Circumstellar disks (235); Planetesimals (1259)

1. Introduction

Stars are born with circumstellar disks of gas and dust, which serve as the cradles for planet formation and evolution. Giant planets are estimated to form within ∼10 Myr before the dispersal of gas in protoplanetary disks (PPDs; I. Pascucci & M. Sterzik 2009), while ice giants and terrestrial planets can continue to grow in the later gas-poor debris disk (DD) phase (P. J. Armitage 2024). Dust in DDs is commonly referred to as second-generation because it primarily arises from collisions between leftover planetesimals that failed to form planets (M. C. Wyatt 2008). Consequently, the dust levels in DDs reflect the subsequent planet formation activity, as large bodies perturb and collide with smaller ones. An effective approach to studying these collisional processes in exoplanetary systems is to analyze infrared emissions from circumstellar dust (i.e., infrared excess) in low-optical-depth systems like DDs, as the amount of dust is directly linked to these processes (S. J. Kenyon & B. C. Bromley 2005). Our solar system has experienced enhanced collisional activity, especially during chaotic phases, including the giant impact that formed the Earth-Moon system (E. Asphaug 2014) and intense bombardment during giant planet migration (R. G. Strom et al. 2005). By integrating infrared observations with theoretical models, researchers have identified a subclass of DDs known as extreme debris disks (EDDs), characterized by exceptionally large (re-emitting more than ∼1% of the stellar luminosity) and time-variable amounts of warm ($\gtrsim$a few hundred kelvin) dust found around only about ∼1% of DDs of similar age surrounding relatively young stars (Z. Balog et al. 2009; G. M. Kennedy & M. C. Wyatt 2013; H. Y. A. Meng et al. 2017). EDDs are thought to represent the chaotic phases occurring within exoplanetary systems.

The substantial warm emissions—coupled with significant variability—link EDDs to the rapid evolution of dust debris in the terrestrial zone. Two key pieces of evidence suggest that large-scale collisions involving large asteroids and planetary embryos give rise to the EDD phenomenon. First, the disk emissions in EDDs display stochastic variability on timescales of months to years, in contrast to the stable emissions observed in typical DDs, which are thought to be sustained by much more frequent collisions among smaller, ∼kilometer-sized planetesimals. Most EDDs are found around stars younger than ∼200 Myr, with about two-thirds exhibiting variable infrared emissions indicative of rapid dust production and clearing (A. Moór et al. 2021). Theoretical studies indicate that violent collisions of large bodies can generate dense debris clouds orbiting the star, leading to complex semiregular variability influenced by viewing geometry and the dynamical and collisional evolution of the debris clouds

Original content from this work may be used under the terms of the Creative Commons Attribution 4.0 licence. Any further distribution of this work must maintain attribution to the author(s) and the title of the work, journal citation and DOI.

(A. P. Jackson & M. C. Wyatt 2012; L. Watt et al. 2024). This "wiggle" behavior in infrared light curves has been extensively documented in three EDDs (K. Y. L. Su et al. 2019; A. Moór et al. 2022). In rare inclined orientations, eclipsing dust clumps have been observed to be comparable in size to the star (e.g., K. Y. L. Su et al. 2022), further validating the scale of these impacts.

Second, EDDs show very prominent solid-state features in the mid-infrared arising from ∼submicron amorphous/crystalline grains. The majority of DDs have infrared spectra that display, at most, only subtle features (C. H. Chen et al. 2006; N. P. Ballering et al. 2014; C. H. Chen et al. 2014), resulting from erosive collisions between smaller, kilometer-sized planetesimals and the rapid loss of small grains due to stellar radiation pressure. Because of the short lifetimes of small grains in DDs, strong spectral features indicate an elevated level of dust-producing collisions. Theoretical simulations suggest that collisions between large, gravity-dominated bodies are violent events that generate powerful shocks, vaporizing a significant portion of the colliding bodies (R. G. Kraus et al. 2012; E. J. Davies et al. 2020). This vapor is expected to quickly condense into dust (B. C. Johnson & H. J. Melosh 2012; B. C. Johnson et al. 2015). These violent impacts are further substantiated by three EDDs that exhibit a distinct ∼9 μm silica feature linked to freshly condensed silica smoke (J. H. Rhee et al. 2008; H. Fujiwara et al. 2012), produced by hypervelocity impacts (C. M. Lisse et al. 2009). In addition to direct vapor condensation, annealing at high temperatures ($\gtrsim$1200 K)—a localized condition resulting from large-scale impacts—can also transform amorphous-silicate material into crystalline forms, such as forsterite (Mg-rich olivine) grains, which have been observed in several EDDs (A. J. Weinberger et al. 2011; J. Olofsson et al. 2012; H. Y. A. Meng et al. 2014). As suggested by A. Morlok et al. (2014b), the mineralogical dichotomy (silica-rich versus forsterite-rich) observed in EDDs may be related to the initial conditions following impacts, as traced by these thermally altered grains. This makes the study of impact-produced dust mineralogy a valuable tool for investigating giant impacts occurring around other stars.

The discovery of EDDs occurred near the end of the Spitzer cryogenic mission; therefore, only a handful of systems with high-quality mid-infrared spectra are available. With the launch of JWST, we are now in a position to further explore the mineralogical dichotomy in EDDs by more than doubling the sample size. In this work, we analyze 16 EDDs using JWST Mid-Infrared Instrument/Medium-Resolution Spectrometer (MIRI/MRS; G. S. Wright et al. 2015) data, with 12 of these having the complete 4.9–27.9 μm mid-infrared spectra obtained for the first time. By including an additional five EDDs observed by Spitzer, we revisit the mineralogical dichotomy (silica-rich versus forsterite-rich) reported in earlier Spitzer studies, and provide a global view of EDD properties linked to impact-produced dust mineralogy, placing them within a broader context compared to earlier PPDs and typical DDs by highlighting three characteristics that define this subclass.

The rest of the paper is organized as follows. The JWST observations, data reduction, and methodology for extracting dust features are briefly discussed in Section 2, with additional details and basic sample properties provided in Appendix A. In Section 3, we explore the unique characteristics observed in EDDs, highlighting elevated amounts of small and thermally altered grains (Sections 3.1 and 3.2), as well as infrared variability (Section 3.3). Further technical details are elaborated on in Appendices B and C. We discuss the broader implications of our findings concerning different phases of planet formation and evolution, comparing them to theoretical expectations in Section 4, and conclude in Section 5.

2. Observations and Results

2.1. Mid-infrared Spectra from JWST and Spitzer

This work reports mid-infrared spectral analysis for 16 EDDs using JWST MIRI/MRS data from the GTO and GO programs (PID 1206—PI Rieke, PID 1282—PI Henning, and PID 3189—PI Su), collectively designed to provide a global view of EDD properties related to impact-produced dust mineralogy. Four of the targets have high-quality mid-infrared spectra obtained by the Spitzer Infrared Spectrograph (Spitzer/IRS; J. R. Houck et al. 2004) ∼20 yr ago, while the remaining 12 have mid-infrared spectra acquired by JWST/MIRI for the first time. Table A1 lists the JWST observations, including the date, on-source exposure time, target identifications, and short names used in the work hereafter. All data were obtained using the MIRI/MRS mode with all four channels and subbands, employing 4-point point-source dithers, resulting in a continuous spectrum ranging from 4.9–27.9 μm. No dedicated background observations were obtained.

We used the JWST Calibration Pipeline version 1.15 (H. Bushouse et al. 2023) and the Calibration Reference Data System context `pmap_1298` to reduce the data using default parameter settings, following the same steps as those in the work of K. Y. L. Su et al. (2025) to flag additional bad pixels. We inspected the source extension (in terms of FWHM) and compared it to that of calibration stars with similar brightness across all spectral cubes and wavelengths, confirming that no significant extended structures were observed around the targets. A 1D spectrum was extracted from each of the cubes using the default aperture of two point-spread function (PSF) FWHMs to minimize resampling artifacts, along with a large sky annulus, both of which increase linearly with wavelengths (D. R. Law et al. 2025).

To provide a better perspective on the dust mineralogy in EDDs, we also analyzed five other EDDs with high-quality mid-infrared spectra from Spitzer/IRS extracted from the CASSIS website (V. Lebouteiller et al. 2011). Although the Spitzer/IRS spectra have much lower spectral resolution than the JWST data, they are sufficient for our analysis method (described below). The basic properties for the whole EDD sample are detailed in Appendix A, including stellar parameters, ages, multiplicity, and the presence of cold dust, with cited references. We use these properties to search for correlations with the observed dust mineralogy—particularly stellar age—to probe evolutionary trends. Figure 1 shows the disk emission after subtracting the stellar contribution for the entire sample.

2.2. Methodology–10 μm Feature Properties

Our objective is to gain a general understanding of the dust mineralogy produced by impacts within a few astronomical units by analyzing the observed 10 μm feature, broadly defined between 7.2 and 13.5 μm. To achieve this, we adopted a straightforward methodology that can be quickly and

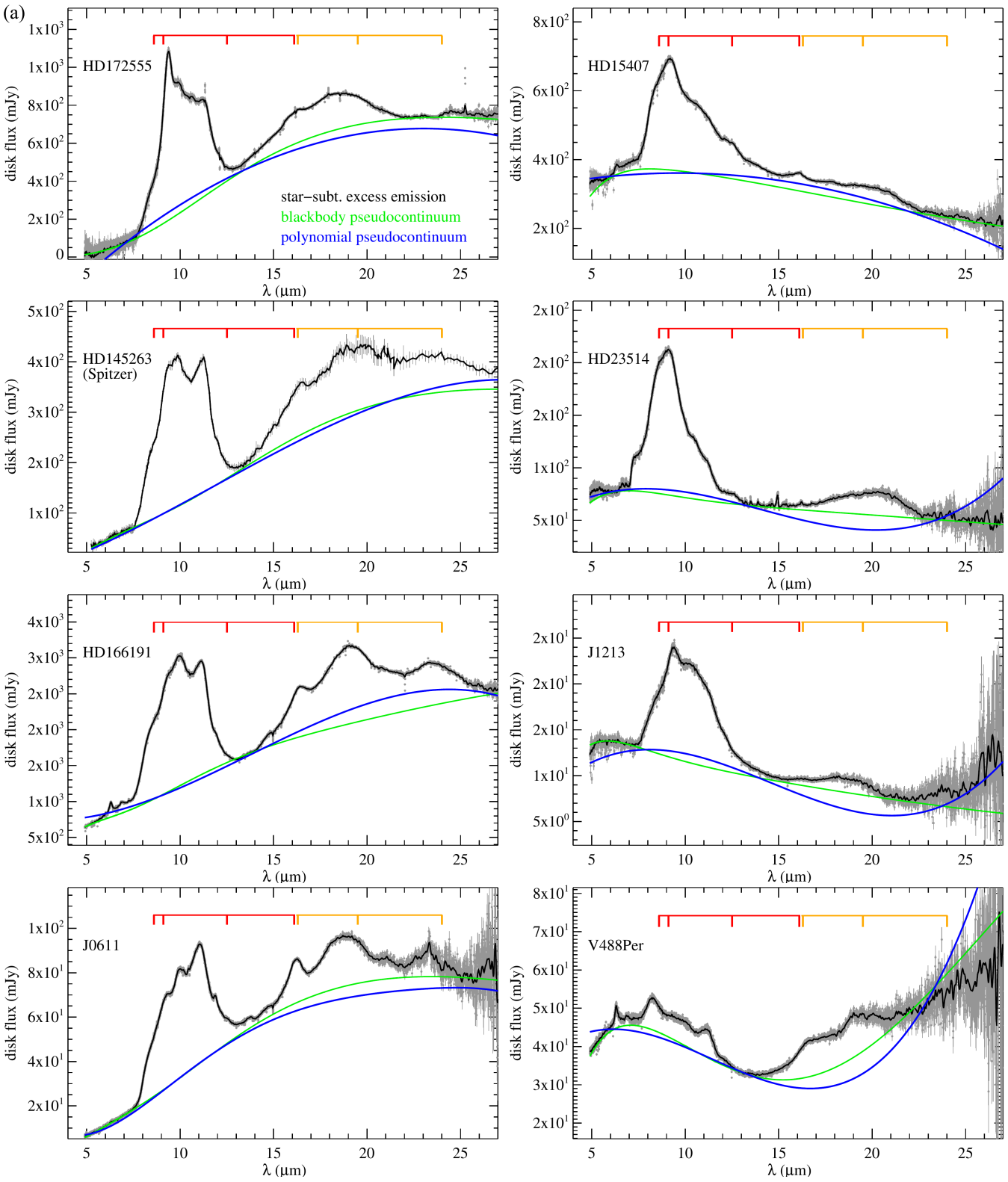

Figure 1. (a) Star-subtracted mid-infrared spectra of the EDDs are shown in black with error bars in gray. JWST MIRI/MRS spectra were binned to $R \sim 300$ for clarity while Spitzer IRS spectra were shown in their native resolution. The two pseudocontinua are shown in green (a combination of blackbody functions) and blue (a polynomial function). The wavelengths for prominent peaks of silica dust are marked on the top in red, while signatures of crystalline olivine (Fe-bearing forsterite) in the 20 μm region are marked in orange. The eight systems shown here are classified as silica-rich EDDs, where the top four are known to be rich in silica dust using Spitzer data, while the bottom four are identified by this work. (b)–(c) Figure 1 for silica-poor systems classified by this work. We note that some systems (J0609, J2301, and V488Per) suffer from poor background subtraction at wavelengths longer than ∼23 μm due to the faintness of the sources and increasing telescope emission.

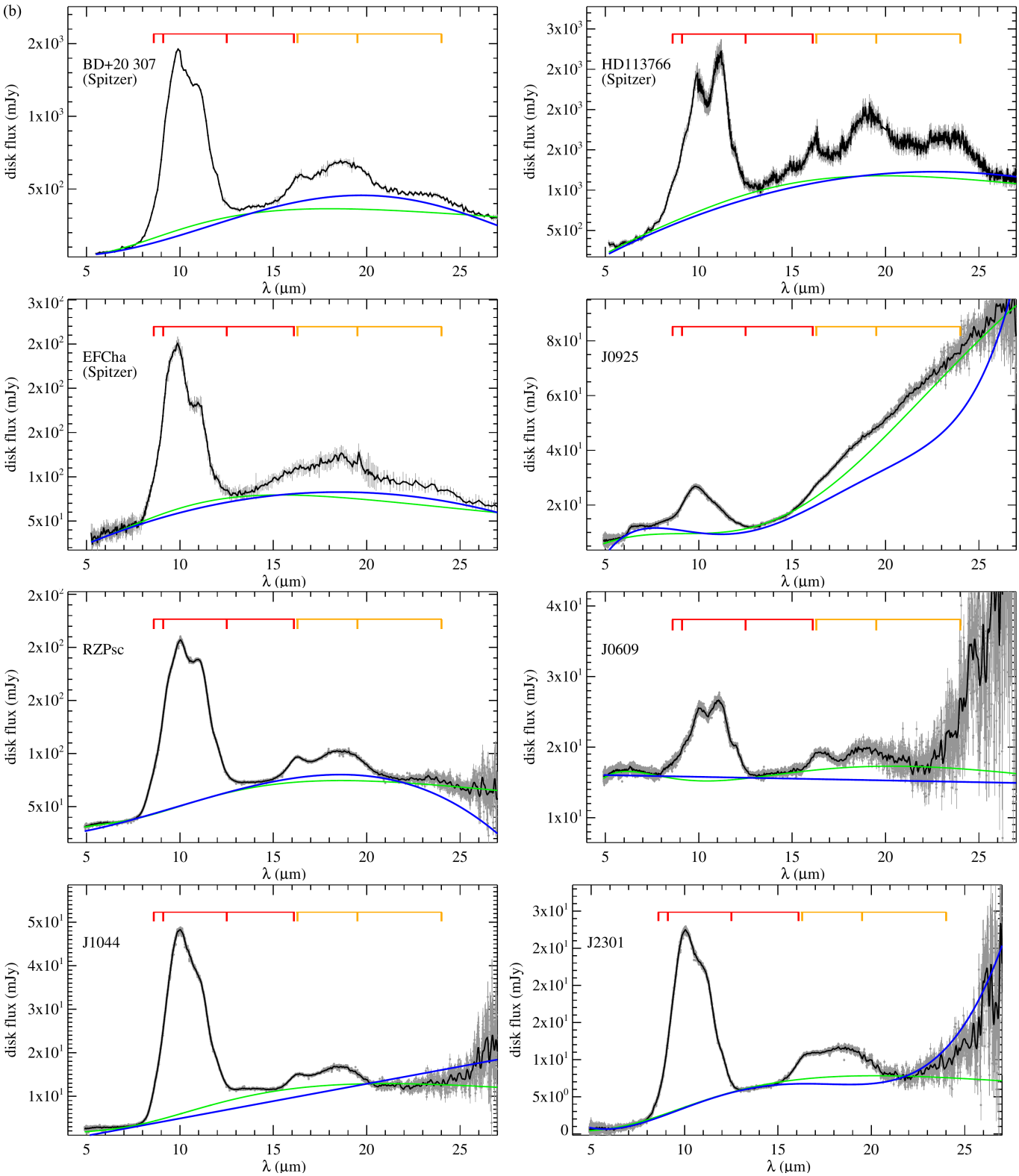

Figure 1. (Continued.)

uniformly applied to a large sample of systems, avoiding debates over the precise features emitted by a given dust composition or mineral. We revisit the silica-rich versus forsterite-rich mineralogical dichotomy by adopting a "dust emissivity" approach to identify systems that show silica-rich signatures in their 10 μm features. The term "emissivity" is not the conventional definition in thermodynamics (a value between 0 and 1); see Appendix B.2 for the definition used in this work. Dust emissivity is defined as the ratio of the feature-producing spectrum to the underlying continuum and

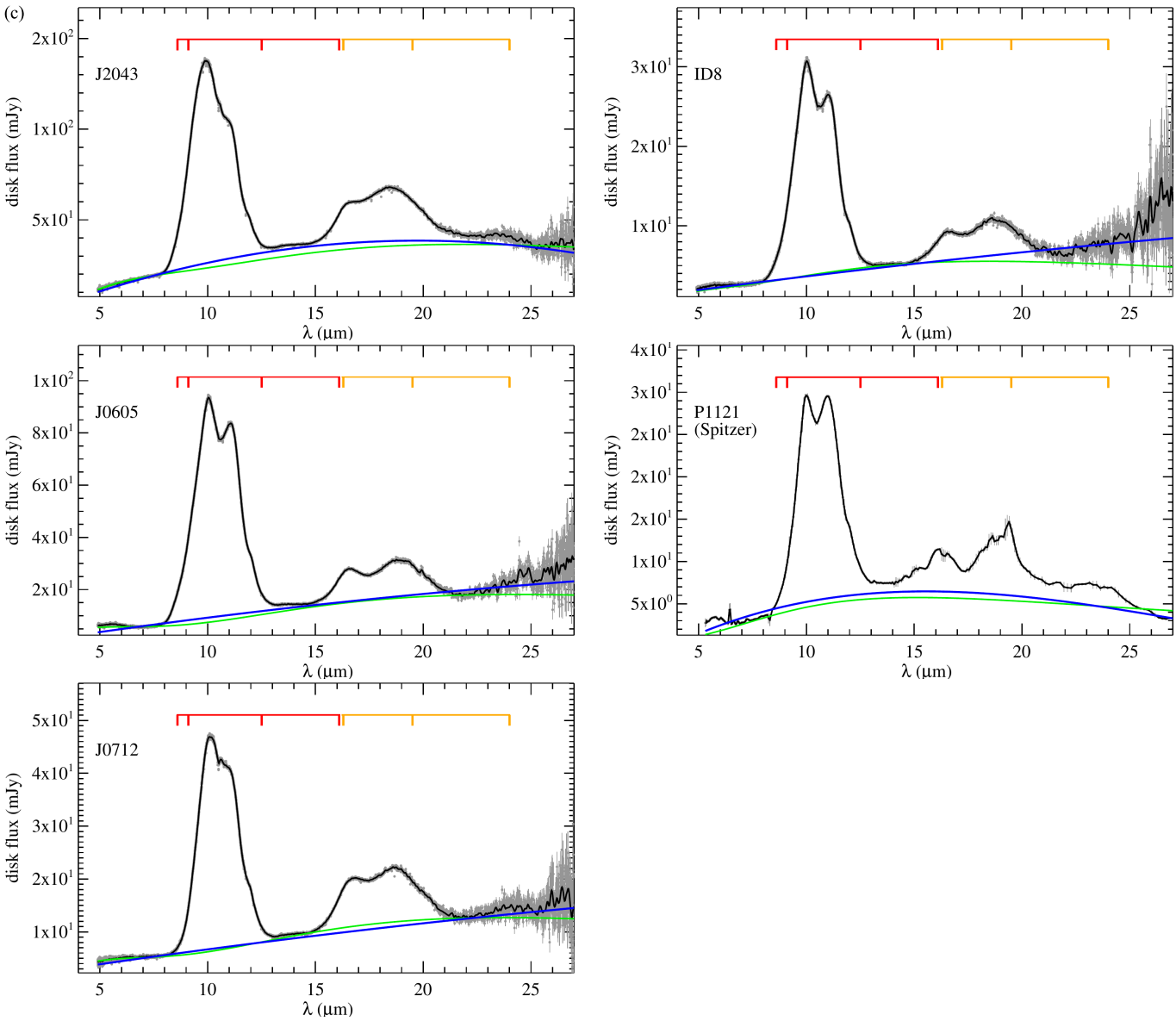

Figure 1. (Continued.)

can be used to reveal the composition of small grains via their distinct solid-state features (e.g., D. M. Watson et al. 2009). Because we focus on dust within a few astronomical units (the terrestrial zone), we restrict our analysis to the 10 μm region, which probes warm dust; its features are less sensitive to grain impurities, structure (e.g., porosity), and continuum placement. The methodology and the rationale for our choices are detailed in Appendix B. The derived dust emissivity in the 10 μm region for the entire sample is shown in Figure B1.

We quantified the properties of the 10 μm dust emissivity using its strength and morphology. The feature strength, referred to as W_{10}, is the equivalent width of the 10 μm feature and serves as a tracer of the amount of optically thin grains (i.e., the total emitting area, which is proportional to the mass) in a system. We also utilized the FWHM and the dust indices of crystalline silicates and silica to quantify the morphology of the feature. The computed FWHM acts as a proxy for the dominant grain sizes and the levels of crystallinity that produce the feature. Generally, the narrower the feature, the smaller the grain size (F. Przygodda et al. 2003; J. Kessler-Silacci et al. 2006). Furthermore, it also reflects the dust's crystallinity; as the width increases, so does the proportion of the crystalline contribution (J. Olofsson et al. 2009; D. M. Watson et al. 2009). We stress that FWHM and W_{10} serve as proxies, but not in an absolute sense (for details, see Appendix B).

Additionally, we employed dust indices to characterize the amount of processed dust in the observed 10 μm dust emissivity. A key aspect of this analysis is defining a pristine 10 μm feature that lacks processed dust and using it as a standard to determine how much an observed spectrum differs by contrasting the specific wavelength range in which processed dust features appear. The greater the contrast (i.e., departure from a nominal value of 1), the more prevalent a specific mineral is in the spectrum (see Appendix B.2 for the mathematical formulation of the defined indices and mineral features). We used the dust emissivity derived from the observed JWST spectrum of LkCa 15 (K. Y. L. Su et al. 2025)

Table 1
Derived Properties of EDDs: 10 μm Dust Indices and Mid-infrared Variability

Object[a]	FWHM (μm)	W_{10} (μm)	P_{10}	O_{10}	S_{10}	$S_{10,s}$	Silica Rich	f_d[b] ($\times10^{-2}$)	4.6 μm Var.[c] Max/Typ.	10/20 μm Var.[d]
HD 172555	1.49 ± 0.01	8.06 ± 1.05	2.01 ± 0.03	1.00 ± 0.03	0.90 ± 0.01	2.95 ± 0.23	Y	0.07	sat.[e]	brightening[f]
ID8	2.13 ± 0.01	15.50 ± 0.27	0.70 ± 0.01	1.28 ± 0.02	0.79 ± 0.06	0.54 ± 0.02	N	2.67	142/41	variable[g]
HD 23514	2.00 ± 0.04	4.43 ± 0.28	2.66 ± 0.06	0.90 ± 0.02	1.77 ± 0.10	8.66 ± 0.25	Y	1.65	31/8	fading[f]
HD 15407	3.22 ± 0.08	2.84 ± 0.04	2.10 ± 0.02	1.30 ± 0.03	5.99 ± 0.49	6.30 ± 0.16	Y	0.66	10/5	fading at $\lambda > 8$ μm
V488Per	3.73 ± 0.01	0.68 ± 0.04	1.40 ± 0.06	1.95 ± 0.10	1.37 ± 0.41	6.53 ± 0.40	Y	16.4	693/198	fading at $\lambda < 8$ μm and W4
J0609	2.22 ± 0.02	1.79 ± 0.08	0.74 ± 0.01	1.95 ± 0.02	2.15 ± 0.01	1.08 ± 0.03	N	15.0	29/8	⋯
J0605	2.25 ± 0.01	23.14 ± 2.77	0.78 ± 0.01	1.32 ± 0.02	1.04 ± 0.02	0.77 ± 0.04	N	3.54	58/15	fading at *N*-band
J0712	2.02 ± 0.01	12.86 ± 0.48	0.51 ± 0.01	1.32 ± 0.02	0.97 ± 0.05	0.16 ± 0.03	N	3.00	25/7	⋯
J0611	3.40 ± 0.02	5.10 ± 0.06	1.49 ± 0.01	1.50 ± 0.01	2.26 ± 0.05	4.11 ± 0.12	Y	5.09	46/11	fading at WISE W3/W4
J0925	2.24 ± 0.04	4.38 ± 0.16	1.00 ± 0.07	0.99 ± 0.09	1.28 ± 0.55	1.56 ± 0.37	N	3.00	173/37	brightening at VISIR
J1044	2.23 ± 0.03	18.69 ± 2.36	1.01 ± 0.02	0.99 ± 0.03	1.13 ± 0.24	1.05 ± 0.01	N	2.43	87/23	⋯
J1213	3.12 ± 0.01	3.08 ± 0.23	1.54 ± 0.03	1.45 ± 0.02	3.51 ± 0.24	3.23 ± 0.10	Y	1.02	21/5	⋯
J2043	2.25 ± 0.01	10.26 ± 0.83	1.03 ± 0.01	1.02 ± 0.02	0.72 ± 0.18	0.94 ± 0.01	N	5.21	20/5	brightening at VISIR
HD 166191	3.34 ± 0.02	4.75 ± 0.08	1.38 ± 0.02	1.33 ± 0.02	0.89 ± 0.14	3.83 ± 0.12	Y	9.15	sat.[e]	variable[g]
RZPsc	2.56 ± 0.01	8.06 ± 0.04	1.10 ± 0.01	1.28 ± 0.01	1.44 ± 0.01	1.51 ± 0.01	N	7.95	72/16	variable[g]
J2301	2.17 ± 0.01	14.80 ± 0.35	0.94 ± 0.01	0.98 ± 0.01	0.62 ± 0.01	0.89 ± 0.05	N	0.65	321/87	fading at $\lambda > 8$ μm
BD+20307[h]	2.25 ± 0.05	14.88 ± 1.87	1.14 ± 0.02	1.05 ± 0.02	0.84 ± 0.02	1.24 ± 0.10	N	3.20	293/57	brightening[f]
P1121[h]	2.12 ± 0.01	11.34 ± 1.11	0.51 ± 0.02	1.49 ± 0.01	1.79 ± 0.10	0.19 ± 0.10	N	2.20	216/49	⋯
HD 113766[h]	2.56 ± 0.01	6.47 ± 0.39	0.98 ± 0.01	1.67 ± 0.01	1.35 ± 0.18	1.89 ± 0.05	N	3.49	sat.[e]	⋯
HD 145263[h]	3.21 ± 0.01	7.93 ± 0.01	1.54 ± 0.01	1.25 ± 0.01	1.07 ± 0.04	3.60 ± 0.06	Y	1.94	25/5	⋯
EFCha[h]	2.18 ± 0.01	6.76 ± 0.46	1.22 ± 0.01	0.94 ± 0.01	0.72 ± 0.13	1.41 ± 0.02	N	0.18	sat.	⋯

Notes.
[a] Object short name is used here, and the full ALLWISE ID is given in Table A1.
[b] The infrared fractional luminosity (f_d) values include the dust feature from the mid-infrared spectra, which are more accurate than the previous estimates based on broadband photometry.
[c] Wide-field Infrared Survey Explorer (WISE) W2 variability in terms of maximum (peak-to-peak) and typical percentages relative to the minimum disk flux.
[d] Comparison between previous 10/20 μm photometry/spectroscopy and the JWST/MIRI/MRS data.
[e] WISE W2 Variability analysis was adopted from the Spitzer/IRAC I2 data (Appendix C).
[f] Based on published studies: K. Y. L. Su et al. (2025) for HD 23514, M. Samland et al. (2025) for HD 172555 and M. A. Thompson et al. (2019) for BD+20307.
[g] Multiple mid-infrared spectroscopic data suggest both brightening and fading behaviors (Appendix C).
[h] Using Spitzer/IRS data.

as the pristine standard and computed the dust indices for three minerals: crystalline olivine (O_{10}), crystalline –pyroxene (P_{10}), and silica (S_{10}), as defined by D. M. Watson et al. (2009). To better characterize silica dust, we introduced a short-wavelength index centered at 8.50 μm ($S_{10,s}$) for quantifying the silica feature, alongside a long-wavelength index (S_{10}) centered at 12.46 μm. Finally, to minimize overlapping features among the three minerals, we reduced the width of the range over which the dust indices were computed compared to the one used in D. M. Watson et al. (2009). The suitability of using LkCa 15 as the pristine reference and associated uncertainty are further justified in Appendix B.3.

The derived 10 μm properties for the combined sample of 21 EDDs, including systematic uncertainties, are summarized in Table 1. To calibrate the dust-index values, we also computed indices for a wide variety of materials with dust absorption opacity measured in the mid-infrared for comparison, including 11 silica-like species, five materials that experienced different degrees of processing, various synthesized materials, and observed and modeled interstellar medium (ISM)-like compositions (Table B1). For a broader context regarding processed dust in circumstellar environments, we also computed the dust indices for a subset of PPDs and DDs to better define the unique properties presented in EDDs. Specifically, we used the silica index on the blue-side shoulder of the 10 μm feature ($S_{10,s}$), derived from silica-like compositions and from silica-rich EDDs and PPDs identified in previous spectral-decomposition studies, to set the threshold for identifying new silica-rich systems (see Appendix B.3 for details). Using this metric, we identify four additional silica-rich systems (V488Per, J0611, J1213, and HD 166191); together with the four previously identified silica-rich EDDs from Spitzer, eight of 21 EDDs (38^{+11}_{-9}%) are silica-rich. Because real dust is a mixture of minerals (different silica polymorphs, varying impurities, and porosities), the labels "silica-rich" and "silica-poor" are relative to the sample and chosen threshold; including or excluding edge cases near the boundary does not affect our overall conclusions (discussed below).

These measured properties, together with other system parameters, are shown in Figures 2 and 3 and are discussed in the next section, which highlights the unique characteristics of EDDs.

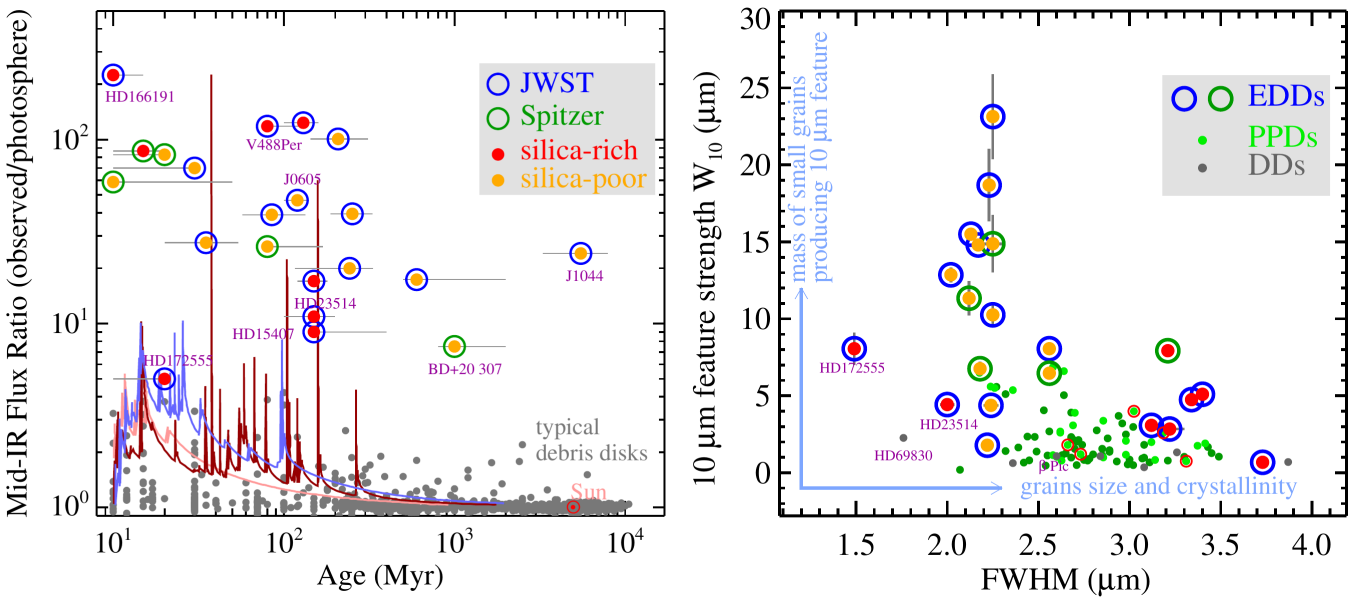

Figure 2. EDD properties in the context of other disks—debris disks (DDs) and protoplanetary disks (PPDs). The left panel shows the evolution of warm dust in DDs, depicting the amount of dust as measured by 22/24 μm flux relative to the star adopted from C. H. Chen et al. 2020. This warm dust is largely depleted as stars age, except in EDDs (large symbols with horizontal bars indicating age uncertainties). The colored lines represent simulated dust evolution models for terrestrial-planet formation (H. Genda et al. 2015), showing that giant impact activities peak at ~10–100 Myr and are significantly reduced after ~300 Myr. The right panel displays the measured width (FWHM) and strength (W_{10}) of the 10 μm feature. In both panels, EDDs rich in silica dust are marked with red dots, while those less so (silica-poor but rich in crystallinity silicates) are marked with orange dots. Measurements for PPDs and DDs are shown as small dots in different colors (gray for DDs; green for PPDs, with dark green indicating the values measured by D. M. Watson et al. 2009).

3. Analysis

3.1. Elevated Amount of Optically Thin Small Grains

EDDs were originally identified by the substantial presence of warm dust surrounding mainly Sun-like stars, which exhibit high mid-infrared fluxes at 22/24 μm, exceeding their stellar emission by a factor of 10 to several hundred (Figure 2, left panel). The large abundance of small grains in EDDs is reflected in the equivalent width of the 10 μm feature, W_{10} (Figure 2, right panel). EDDs have much higher W_{10} values than those of PPDs and DDs. The prominence of the 10 μm feature largely depends on grain sizes and emitting temperatures. Smaller grains display sharper features than the muted characteristics of larger grains. Furthermore, when exposed to the same radiation field, smaller grains heat to higher temperatures than their larger counterparts (P. A. Aannestad & E. M. Purcell 1973; E. Kruegel 2003), resulting in decreased relative feature strengths between 10 and 20 μm as temperatures drop (see Figure D1 of K. Y. L. Su et al. 2025). In PPDs, W_{10} values are constrained by the optically thin disk atmosphere, despite having higher dust content. Consequently, achieving large W_{10} values in PPDs is challenging, except in cases of extremely flared disks or those with large inner holes (e.g., PDS 70; H. Jang et al. 2024b). When a measurable 10 μm emission feature appears, it must originate from relatively optically thin conditions.

It is widely recognized that the dominant grain size responsible for the 10 μm feature in PPDs (i.e., grains in the low-optical-depth disk surface) is of the order of a few microns (I. Oliveira et al. 2011; J. Varga et al. 2026), likely due to a balance between grain growth, fragmentation, and vertical mixing in a gas-rich environment (T. Birnstiel et al. 2010). As noted earlier, the measured FWHM not only reflects the grain size but also indicates the fraction of mixed crystalline silicates in composite porous particles (N. V. Voshchinnikov & T. Henning 2008). Interestingly, roughly one-third of the EDDs have large FWHMs that overlap with the extensive FWHM range observed in PPDs (Figure 2). As shown in the next subsection, these EDDs are rich in both silica and crystalline silicates, resulting in a broader FWHM. In other words, the measured FWHMs indicate that the solid-state features of the majority of EDDs are produced by grains smaller than those in PPDs (i.e., submicron-sized grains).

Low W_{10} values in DDs are understandable, as grains experience collisional destruction followed by rapid loss due to radiation pressure in a low-optical-depth environment. Typical DDs rarely exhibit prominent 10 μm solid-state features, consistent with a paucity of warm, small grains. The reason for this is twofold: either they lack small grains, or the grains are too cold, situated tens of astronomical units away from the star. When the dust temperature falls below a few hundred degrees (i.e., beyond a few astronomical units), the bulk emission shifts toward longer wavelengths. Consequently, the 10 μm feature becomes weaker, even in the presence of small grains. The prominence of the solid-state feature in EDDs suggests that the emission arises from optically thin small grains within a few astronomical units, which are subject to rapid loss if they are smaller than the sizes affected by radiation pressure blowout. Almost all EDDs in our sample show elevated small-grain populations (measured by W_{10}), consistent with recent large dust-producing collisions (between bodies $\gtrsim$ a few hundred kilometers) occurring within the terrestrial-planet formation zone. That phase is expected to wane after a few hundred Myr, consistent with only three known EDDs older than 300 Myr among our 21 systems (left panel of Figure 2); implications of the old EDDs are discussed in Section 4.

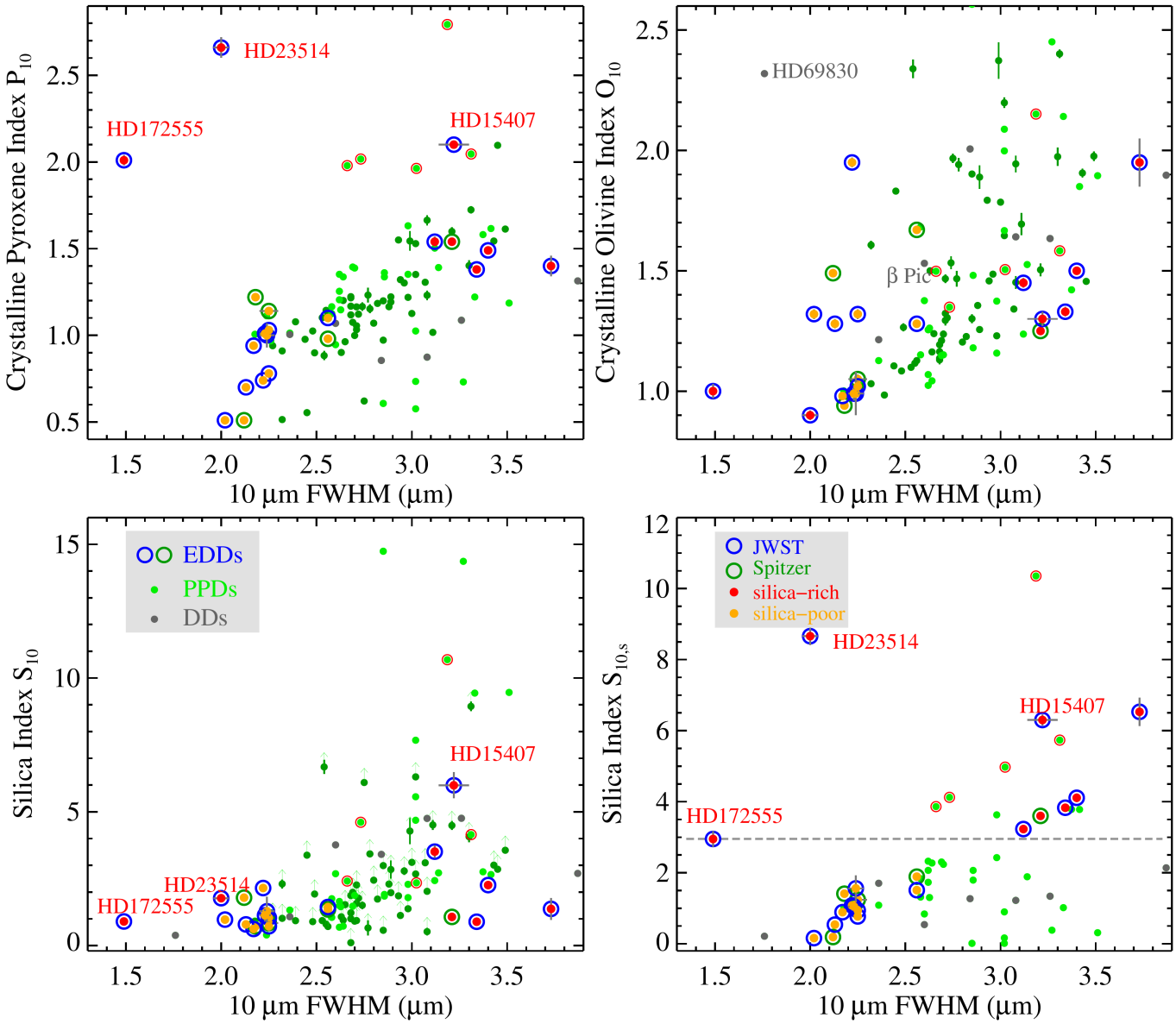

Figure 3. Dust indices in the 10 μm region: P_{10} and O_{10} (upper two panels) for crystalline silicates and S_{10} and $S_{10,s}$ (lower two panels) for silica, for EDDs, and a selected sample of PDDs and DDs (smaller dots). The PPD indices from D. M. Watson et al. (2009) are shown in dark green and marked with upward arrows in the S_{10} panel since they were computed using a wider wavelength width (see Appendix B.2). Thin, red circles mark the five silica-rich PPDs from B. A. Sargent et al. (2009a). The horizontal dashed line in the $S_{10,s}$ panel marks the thresholds for silica-rich systems.

3.2. Elevated Amount of Thermally Altered Grains

Among a handful of EDDs discovered by Spitzer, there appears to be a mineralogical dichotomy in the impact-produced dust: silica-rich versus forsterite-rich (H. Y. A. Meng et al. 2015). Classic examples of silica-rich EDDs include HD 172555 (C. M. Lisse et al. 2009), HD 15407 (H. Fujiwara et al. 2012), and HD 23514 (J. H. Rhee et al. 2008), all characterized by a prominent $\sim$9 μm feature likely produced by vapor condensates resulting from hypervelocity collisions between planetary embryos (B. C. Johnson et al. 2012). Forsterite-rich systems such as ID8 and P1121 (J. Olofsson et al. 2012; K. Y. L. Su et al. 2019) are interpreted as thermally annealed products of amorphous silicates transforming into crystalline silicates, primarily forsterite (Mg-rich olivine), at high temperatures (D. Fabian et al. 2000; S. P. Thompson et al. 2019). Comparative studies of dust mineralogy in meteorites (A. Morlok et al. 2014a) suggest that while both types are highly processed and have experienced intense heating, silica-rich materials are more highly shocked, whereas forsterite-rich materials are less so (A. Morlok et al. 2014b). It is interesting to note that the gas-phase condensation temperature for silica-like materials is typically around 1200–1800 K and can reach up to a couple thousand kelvin at high pressures. In contrast, for forsterite, the temperature typically ranges from 1000–1200 K, suggesting that the events responsible for the production of silica are typically more energetic (resulting in higher temperatures) than those for forsterite.

With 12 additional high-quality JWST mid-infrared spectra of EDDs, we can now reassess the apparent dichotomy in impact-produced mineralogy by comparing the relative amounts of highly processed dust. Figure 3 presents four dust indices for the 21 EDDs alongside values for selected PPDs

and DDs; we use the PPD indices to provide global context for thermally processed dust in EDDs. Spectral decompositions of Spitzer PPD spectra show that dust in the disk surface layer has ∼10%–40% crystallinity by mass fraction (B. A. Sargent et al. 2009b; I. Oliveira et al. 2011). Although most PPD studies focus on Mg-rich crystalline silicates (enstatite and forsterite), silica (amorphous quartz) contributes a comparable mass fraction in some systems (B. Sargent et al. 2006; J. Olofsson et al. 2010; I. Oliveira et al. 2011); a small subset (five of ∼80 PPDs) shows distinct features at ∼9, 12.6, and 20 μm attributed to crystalline silica (B. A. Sargent et al. 2009a). EDDs exhibit a similar spread in dust indices to PPDs, suggesting that the prominent 10 μm features are dominated by thermally processed dust. As detailed in Appendix B.3, we use the $S_{10,s}$ index—calibrated from previously identified silica-rich systems—to select silica-rich objects. In both PPDs and EDDs, silica-rich systems preferentially occupy the high-P_{10} region, while the O_{10} and S_{10} distributions are more mixed. Another interesting observation from these dust indices is the positive correlation between $S_{10,s}$ and the combined crystalline silicate indices ($\sqrt{P_{10}^2 + O_{10}^2}$, Figure B4). All silica-rich systems, including PPDs, exhibit high crystallinity, reflecting the fact that they are all highly processed materials.

The varying proportions of silica polymorphs mixed with other crystalline silicates complicate accurate identification. This highlights the limitation of using only the 10 μm region for dust-index analysis; extending the analysis to the ∼20 μm region also faces challenges, because feature positions and strengths are highly sensitive to composition (Al/Mg/Fe ratios) and grain porosity, introducing additional degeneracies that future spectral-decomposition frameworks must address. Instead of using the original dichotomous terminology, we classified the EDD dust mineralogy as silica-rich versus silica-poor, with the latter representing the initial forsterite-rich classification. Although we classify systems into two broad themes based on the observed mineralogy, it is evident that there exists a wide spectrum of dust compositions and varying levels of mixing in all circumstellar environments. In our broad definition, a silica-rich system is one where the observed features resemble those of silica dust with sufficient abundance (greater than the typical values observed in PPDs). This does not necessarily imply that silica-rich systems lack any forsterite or enstatite dust, or vice versa (see detailed comparison in Appendix B.3). Our goal is to identify EDDs enriched in silica dust and to uncover their implications by correlating them with other characteristics of EDDs. Based on the threshold of the $S_{10,s}$ silica index, 38^{+11}_{-9}% of EDDs (eight out of 21) are classified as silica-rich, while fewer than 10% of PPDs (6^{+4}_{-2}%; five out of ∼80; see Appendix B.3) fall into the same category using Spitzer data.[9] This likely suggests an enrichment of silica dust in EDDs compared to the precursor material found in PPDs, implying that advanced thermal processes in EDDs play a crucial role in the formation of silica dust. As shown in the left panel of Figure 2, both types of dust mineralogy are found around EDDs associated with stars younger than 300 Myr, while only silica-poor EDDs are observed around older stars (though the sample size is small). Another interesting feature revealed in the right panel of Figure 2 is that silica-poor systems tend to have relatively large W_{10} values, indicating a greater mass of the optically thin small grains. We will explore the implications of these findings in Section 4.

3.3. Infrared Variability

Infrared variability resulting from changes in the emitting area (i.e., total dust cross section) greater than a few times the stellar size is another hallmark commonly observed in EDDs. Put in perspective, the required total cross-sectional area for $f_d = 0.01$ at 1 au is roughly 3×10^{25} cm^2; therefore, 10% variations require changes to the area of $\pm 3 \times 10^{24}$ cm^2. Both short-term (weekly to monthly) and long-term (yearly) variations are recognized (K. Y. L. Su et al. 2019; A. Moór et al. 2021). Dedicated monitoring by the warm Spitzer mission, using 3–5 μm photometry for a sample of two dozen EDDs, shows that most variations are stochastic (G. H. Rieke et al. 2021; K. Y. L. Su et al. 2022, 2023, 2025), while only three systems exhibit significant semiregular monthly modulations in their infrared light curves (ID8, P1121, and TYC 4209-1322-1; K. Y. L. Su et al. 2019; A. Moór et al. 2022). The "wiggly" nature in these EDDs is related to the complex, dynamical, and collisional interplay between the brighter vapor condensates initially and the fainter boulder-grinding disks that emerge later following a violent impact (K. Y. L. Su et al. 2019; L. Watt et al. 2024). In rare highly inclined systems, irregular optical transit profiles are observed as large dust clumps, formed in the aftermath of a major impact, pass in front of the star (E. Gaidos et al. 2019; C. Melis et al. 2021; K. Y. L. Su et al. 2022, 2023; M. Kenworthy et al. 2023; N. L. Zakamska et al. 2025).

We focused on long-term behaviors by conducting an analysis of the general infrared variability around these EDDs, utilizing Wide-field Infrared Survey Explorer (WISE) and other mid-infrared photometric data. WISE 3–5 μm photometry tracks the evolution of warm dust every 6 months between 2014 and 2024, while 10/20 μm photometry from IRAS, Spitzer, AKARI, Midcourse Space Experiment (MSX), and/or ground-based Very Large Telescope (VLT), Gemini, and Subaru monitors the evolution of silicate features over several decades. The variability behavior for each of the objects is detailed in Appendix C. Since infrared observations directly track variations in the debris cross sections (constraining the minimum change required), we aim to connect the observed dust mineralogy with disk variability to investigate potential correlations.

For each system, we derived two indicators to represent the relative infrared variability using WISE 4.6 μm data[10] (see Table 1): the maximum and typical variations relative to the minimum disk flux at 4.6 μm, which is assumed to be the nominal background flux level sustained by collisions among existing small planetesimals. The typical variation reflects the stochastic nature of collisions, while the maximum variation represents the greatest degree of change observed in the data over the monitored period. As detailed in Appendix C.1, we find that the two variability indicators are strongly correlated, suggesting that they are likely driven by a common physical process related to the aftermath of giant impacts. The observed

[9] J. Varga et al. (2026) analyzed 26 PPDs with high-quality JWST data, finding annealed (i.e., crystalline) silica in nine systems—a fraction of 35^{+10}_{-8}%. They emphasize that such robust detections require high signal-to-noise JWST data. The incidence of silica-rich PPDs is not the focus of this study and has no impact on our general conclusion.

[10] Several systems are saturated in the WISE W1/W2 data, so we adopted archival Spitzer I1/I2 data instead.

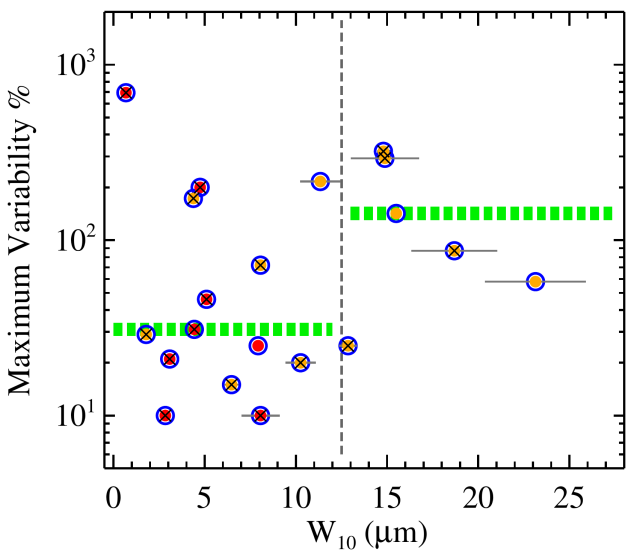

Figure 4. Correlation between the observed 4.6 μm disk variability (y-axis) and EDD properties: W_{10} (x-axis), impact-dust mineralogy (red: silica-rich; orange: silica-poor), and multiplicity (crosses). Dividing EDDs by W_{10} shows a potential trend: high-W_{10} ($\gtrsim$12.5 μm) systems—exclusively silica-poor—tend to exhibit greater variability (a factor of $\sim$5), as indicated by the median values (green dashed lines).

flux change can also be expressed as the minimum change in dust cross section ($\Delta\Sigma$) required to match the maximum flux change under the assumptions that (1) the emission is optically thin and (2) all dust is at the same temperature. Using the warmer temperature used in the pseudocontinuum, we found that $\Delta\Sigma$ ranges from to 2.7–233 times that of the stellar surface (assuming a size comparable to the Sun) in our sample (details see Appendix C.1), suggesting that the variation originates from the circumstellar environment rather than from the star or any emerging planetary bodies.

We observe no strong correlation between disk variability, as measured by both relative flux change and dust cross section, and factors such as derived dust indices, stellar age, and multiplicity (Figure C2). In systems younger than 300 Myr ($\sim$85% of the sample), we observe a diverse range of variability levels and dust mineralogy. Older systems (age $>$300 Myr) seem to occupy a region of greater variability compared to younger EDDs; however, the sample size of older systems is small (only three). The only correlation we identified is that high-W_{10} systems (a proxy for the mass of optically thin small grains), which are exclusively silica-poor, tend to exhibit greater variability by a factor of 5 as measured in the relative flux space (Figure 4), but not in the dust cross section (Figure C2). This trend is unlikely to be related to age, as no correlation is observed between stellar age and silica-poor systems. We will explore this further in Section 4.

Multiplicity is a notable characteristic of EDDs, indicating that most EDDs have one or more companions at varying separations—close (within a few astronomical units), intermediate (tens of astronomical units to 500 au), or wide ($>$500 au; details in Table A2). Nonetheless, our search for correlations between multiplicity and EDD properties revealed no significant trends. Notably, three older EDDs (over 300 million years) with high-W_{10} values are found in wide binary systems with high eccentricity, but not all high-W_{10} EDDs have stellar companions. Due to the small sample size, the influence of multiplicity on EDD phenomena remains unclear. Future research would benefit from a larger sample, especially with older EDDs and more precise binary property assessments.

Given that the time sampling for the 10/20 μm observations varies across different sources (depending on brightness), we focus on comparing the synthetic photometry derived from the JWST/MIRI/MRS spectrum with existing photometry from IRAS, AKARI, Spitzer, MSX, and ground-based mid-infrared cameras. This comparison allows us to characterize EDDs as exhibiting fading, brightening, or both behaviors at 10/20 μm (Table 1). As detailed in Appendix C.2, all three behaviors are found, although the fading behavior is detected more frequently than the other two (Figures C3 and C4). This behavior aligns with the identification criteria for EDDs, which are exceptionally brighter than the general population, suggesting that this phenomenon is associated with the aftermath of an abrupt past event. Except for a few cases where significant brightening events were recorded in the last decade with sufficient infrared temporal data, most major impacts in EDDs occurred prior to their discovery (e.g., K. Y. L. Su et al. 2022; M. Kenworthy et al. 2023). We also find no dramatic changes in the morphology of the 10 μm feature over several decades, with variations primarily attributed to the underlying continuum rather than the dust composition, although subtle changes may still occur (Figure C3). This overall stability is consistent with earlier studies (M. A. Thompson et al. 2019; K. Y. L. Su et al. 2020, 2025; M. Samland et al. 2025). Similar to the 4.6 μm WISE data, there is no significant correlation between 10/20 μm variability behavior and dust mineralogy, regardless of whether the dust is silica-rich or silica-poor.

4. Implications

The implications of our results are summarized and illustrated in Figure 5, where the three different phases of planet formation and evolution—giant planet formation prior to the dispersal of nebular gas, terrestrial-planet formation through planetesimal/embryo collisions, and orbital instability due to the rearrangement of giant planets or other late instabilities—are roughly categorized by the system's age. While PPDs establish the initial conditions for giant planet formation, EDDs offer the best insight into the dynamically active stages during terrestrial-planet formation and subsequent planetary evolution, particularly through the properties of highly processed materials. Although both silica and crystalline silicate dust have undergone significant processing and intense heating, silica-rich materials exhibit higher shock levels than the others (referred to as silica-poor), particularly the forsterite-rich materials, as noted by A. Morlok et al. (2014a, 2014b). Because impact energy strongly depends on mass, we suggest that silica-rich EDDs tend to arise from collisions between large planetary embryos (similar in size to Mars), while silica-poor EDDs result from less energetic events likely involving somewhat smaller bodies (approximately the size of the Moon). Notably, silica-rich EDD systems are exclusively observed around stars younger than $\sim$300 Myr, consistent with the findings of numerical simulations on terrestrial-planet formation, as the giant impact phase is expected to significantly diminish after a few hundred million years (J. E. Chambers 2013; E. V. Quintana et al. 2016).

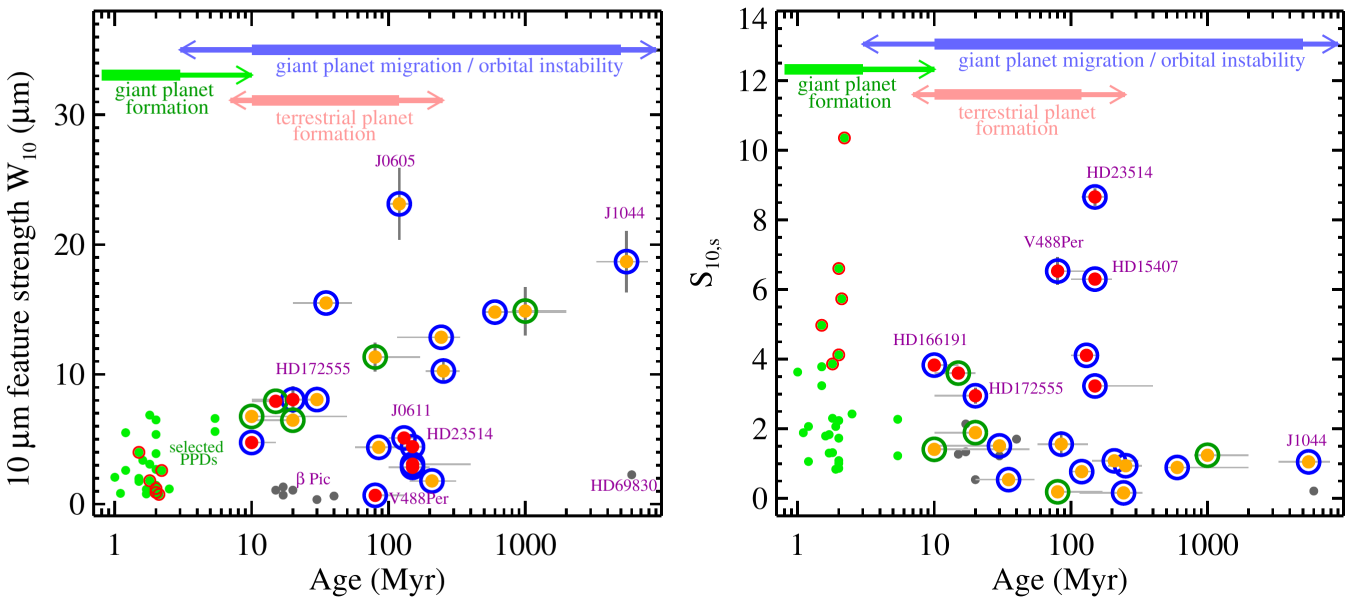

Figure 5. The 10 μm feature strength (left) and abundance of silica dust (characterized by $S_{10,s}$, right) are shown at three different stages of planet formation and evolution: giant planet formation, terrestrial-planet formation, and the giant planet migration/orbital instability period, which are indicated at the top of each panel. Symbols and colors are the same as in Figure 2. Both types of silica-rich and silica-poor EDDs are found during the terrestrial-planet formation phase, but no silica-rich systems are found in stars $\gtrsim$300 Myr despite their relatively large W_{10}, implying that collisions induced by orbital instability are less violent but more frequent at ages <300 Myr. High abundance of silica dust is only associated with the EDDs corresponding to the terrestrial-planet formation phase.

Terrestrial-planet formation is a messy, complicated process. Impact simulations demonstrate a broad spectrum of outcomes that depend on factors such as collision type (head-on versus grazing), impact velocity, and impactor sizes (S. T. Stewart & Z. M. Leinhardt 2012), and the presence or absence of giant planets (P. J. Carter et al. 2015; P. J. Carter & S. T. Stewart 2020). Therefore, it is not surprising to observe a mixture of silica-rich and silica-poor EDDs during the terrestrial-planet formation era. Although the smallest size of debris clumps that can be tracked in impact simulations is much larger than the dust observed through astronomical observations, these simulations can provide a zero-order estimate of the spatial distribution of the resulting debris. Recent studies (S. Cambioni et al. 2019; A. Emsenhuber et al. 2024) indicate that events involving low-mass (less than Mars-sized) impacting bodies are more likely to generate numerous debris clumps, while high-velocity impacts (greater than $\sim$40 km s^{-1}) produce fewer clumps, likely due to the stronger shocks or vaporization that occur under such conditions, which inhibit debris formation. Our findings are consistent with these theoretical expectations, as silica-rich EDDs typically exhibit relatively low W_{10}, which is attributed to a smaller amount of optically thin small dust. The abundance of silica dust as traced by the $S_{10,s}$ index in EDDs peaks at a few hundred million years (as shown in the right panel of Figure 5), providing strong observational support for the occurrence of planetary-embryo collisions (i.e., the final phase of giant impacts) in theoretical studies.

We further suggest that the relative abundance of silica dust compared to nonsilica dust (such as crystalline silicates) might indicate how long it has been since the initial giant impact that created the silica dust. After a giant collision, a new belt of resulting remnants (objects smaller than the original bodies) is expected to form. Subsequent collisions in the belt likely produce silica-poor material, as these impacts are generally less energetic than the original, as typically found in impact simulations. This speculation would only hold if both types of dust have similar lifetimes against radiation pressure blowout, as subsequent dust dynamics could erase the initial imprint.

We propose that silica dust in the silica-rich EDDs forms from direct gas-phase condensation resulting from high-energy impact events. Such energetic impacts are expected to vaporize a significant fraction of the impacting bodies (E. J. Davies et al. 2020), resulting in the formation of droplets that condense from rapidly cooling gas. These condensed materials —known as spherules—have been identified in impact products preserved in terrestrial and lunar craters (J. Smit 1999; B. C. Johnson & H. J. Melosh 2014). In this case, the expansion of the vapor quickly cools the gas and should preferentially form silica in low ambient pressure as amorphous polymorphs such as silica glass, obsidian, or fused quartz. Grinding down the freshly condensed spherules into submicron dust occurs rapidly in the dense, impact-produced cloud (B. C. Johnson et al. 2012; K. Y. L. Su et al. 2020). This is consistent with the observation that obsidian and fused quartz are the matching minerals that can reproduce the observed spectra of HD 172555 and HD 15407 (C. M. Lisse et al. 2009; H. Fujiwara et al. 2012). For less energetic events, in addition to direct gas-phase condensation, annealing may play an important role in forming crystalline silicates; specifically, Mg-rich forms like forsterite (C. Davoisne et al. 2006). Interestingly, there exists an antagonistic relationship between quartz (crystalline silica) and forsterite —pairs of minerals that rarely or never coexist in igneous rocks in the early Hadean Eon (R. M. Hazen et al. 2023). Given the prominence of the features, it is unlikely that the apparent dichotomy (silica-rich versus silica-poor/forsterite-rich) is geologically related to newly formed magma oceans, as these highly processed grains likely formed in interplanetary space—due to rapid cooling of expanding vapor—rather than on planetary surfaces. A key test for silica formed in expanding vapor condensates will be the scarcity of high-

pressure polymorphs such as coesite and stishovite. Future spectral-decomposition analysis of these newly identified silica-rich EDDs will further test this hypothesis.

Our analysis also reveals that silica-poor systems are preferentially linked to higher W_{10} values (as shown in the left panel of Figure 5), where large W_{10} values imply a more widespread distribution of optically thin debris. Notably, all three older EDDs, which exist beyond the era of terrestrial-planet formation, exhibit very high-W_{10} values and are silica-poor. These old EDDs likely resulted from planet migration and the rearrangement of an earlier established planetary system, triggered by a late dynamical instability due to planet–planet and planet–planetesimal interactions (S. N. Raymond et al. 2010; K. Volk & B. Gladman 2015; B. Quarles & N. Kaib 2019) or by tidal evolution of planet–satellite interactions (B. M. S. Hansen 2023). The former cases might be analogous to proposals for a Late Heavy Bombardment in the solar system, when the gas giants migrated outward, creating a more chaotic environment that disturbed smaller bodies and sent them toward the inner terrestrial zone (R. Gomes et al. 2005; R. G. Strom et al. 2005; W. F. Bottke & M. D. Norman 2017). The latter case might be similar to how some of the moons formed around Saturn (E. Asphaug & A. Reufer 2013; M. Ćuk et al. 2016).

Interestingly, recent studies of the solar system suggest that the orbital instabilities shaping its final planetary architecture may have occurred earlier than previously expected (D. Nesvorný et al. 2018; B. Liu et al. 2022). In parallel, studies of mature multiplanet systems observed in transit reveal a similar picture. Resonant chains of planets, which are expected to form during gas-disk-driven migration (e.g., A. Izidoro et al. 2017; K. H. Wong & M. H. Lee 2024, and references therein), are nearly universal among the youngest systems but are progressively dissolved with age. This "breaking-the-chain" process is reflected in the decline of near-resonant configurations from $\gtrsim$80% (<100 Myr) to ∼40% (100 Myr–1 Gyr) and $\lesssim$25% (>1 Gyr), implying a characteristic disruption timescale of ∼100 Myr (F. Dai et al. 2024; J. H. Hamer & K. C. Schlaufman 2024). A range of mechanisms has been proposed to drive this evolution (A. Izidoro et al. 2017; S. T. S. Poon et al. 2020; M. Goldberg & K. Batygin 2022; C. Charalambous et al. 2025; R. Li et al. 2025), including interactions with leftover planetary embryos as well as residual planetesimal populations (M. Goldberg & A. C. Petit 2025; J. Li et al. 2026; M. Ogihara & M. Kunitomo 2025). The coincidence of this timescale with the observed peak in the incidence of EDDs raises the possibility that EDDs might also be an observable byproduct of the same dynamical instabilities that reshape planetary system architectures.

Additional evidence linking the EDD phenomenon to dynamical instability—rather than terrestrial-planet formation—arises from the observed disk variability. As shown in Figure 4, EDDs with high W_{10} ($\gtrsim$12.5 μm) tend to exhibit greater variability at 3–5 μm by a factor of 5—as indicated by the median values for the $W_{10} \gtrsim 12.5$ μm and $W_{10} \lesssim 12.5$ μm groups. The combination of high W_{10} and the degree of variability suggests that these large W_{10} systems are undergoing significant collisional activities. Furthermore, the fact that they are all silica-poor systems implies that these collisional activities are predominantly driven by minor bodies and/or less energetic grazing events. This is consistent with the fact that hit-and-run type of collisions are most commonly found during dynamical instability (T. Ghosh et al. 2024; S. Cambioni et al. 2025). Our findings align with the results from Y. Wu et al. (2024) and R. Li et al. (2025), which demonstrate that minor mergers between debris and resonant planets play an important role in enhancing the asymmetry of the departure from exact commensurability between neighboring planets. In this context, silica-poor EDDs with very high-W_{10} values may serve as indicators of dynamical instabilities that ultimately shape the final architecture of planetary systems. This intriguing hypothesis can be further tested with a larger sample of high-quality JWST data, particularly by expanding the focus to include older EDDs.

In closing, we briefly discuss two circumstellar disks outside our sample that may or may not be related to the EDD phenomenon. We do not classify the HD 69830 system as an EDD due to its relatively low dust levels and lack of variability. This 4–10 Gyr-old star, which hosts three super-Earth-sized planets (likely in a chain of mean-motion resonances within 0.63 au; C. Lovis et al. 2006) and that are packed inside a highly stirred DD at ∼1 au (M. C. Wyatt et al. 2007), would have been classified as an EDD in its past. Currently, its debris is approximately 1400 times more luminous than the zodiacal emission in our solar system, exhibiting high crystallinity from small grains (C. A. Beichman et al. 2011). This contrasts sharply with the properties of our solar system's zodiacal cloud, which is dominated by grains of a few 100 μm in size. Several theoretical studies have explored its formation pathways (Y. Alibert et al. 2006; M. J. Payne et al. 2009), making it one of the successful examples in the context of "breaking-the-chain" instability where the three super-Earths locked into orbital resonances as they are today. We stress that the EDD phenomenon can arise from various mechanisms, including the formation of circumplanetary rings resulting from collisions or tidal disruptions of satellites orbiting giant planets. Notably, a recent observation has identified a giant, gas-rich circumplanetary ring occulting the Gyr-old main-sequence star ASASSN-24fw, where its significant infrared excess of warm dust may qualify it as an EDD (N. L. Zakamska et al. 2025; S. Shah et al. 2026). The size of the ring is similar to that of Saturn's largest dusty ring, discovered by Spitzer (A. J. Verbiscer et al. 2009). Its exact connection with the EDD phenomenon requires further investigation.

5. Conclusion

We examined a sample of 21 EDDs with high-quality mid-infrared spectroscopic data (Section 2) to enhance our understanding of the relationship between dust mineralogy and EDD properties (Section 3). This includes disk variability, which reflects the dynamical state following major impact events (Appendix C), and stellar age, which signifies the different stages of planet formation and evolution (Section 4). Our findings suggest that EDDs consistently contain a significantly higher amount of low-optical-depth dust grains compared to the typical levels observed in PPDs and DDs (Appendix B.3). These grains are predominantly submicron in size, whereas PPDs are primarily dominated by micron-sized grains. Additionally, our analysis reveals that silicate dust in EDDs exhibits high crystallinity in both pyroxene and olivine, similar to that found in PPDs, indicating that it has undergone advanced processing compared to primordial ISM-like material. The high crystallinity in silicates observed in PPDs has been recognized for decades and is mainly attributed to

thermal alterations resulting from rapid heating and cooling in gas-rich environments (see references in H. Jang et al. 2024a). We argue that the high crystallinity observed in EDDs is not inherited from early-stage PPDs; if it were, we would have observed similar crystallinity in DDs. Instead, this high crystallinity is generated anew during recent transient violent events, as evidenced by the combination of short loss timescales and large quantities.

In addition to the large quantity of small grains (traced by the equivalent width of the 10 μm feature W_{10}), another important factor that distinguishes EDDs from PPDs is the abundance of silica dust. One-third of the EDDs ($\sim$38%) exhibit significantly elevated levels of silica dust, which tend to broaden the measured FWHM of the 10 μm feature (Appendix B.3). Four dust indices, P_{10}, O_{10}, S_{10}, and $S_{10,s}$, are used to quantify the 10 μm dust morphology, with the former two describing the silicate dust crystallinity and the latter two addressing the silica fraction. By benchmarking dust indices measured from natural silica-rich materials and previously identified silica-rich systems, we categorize the EDD sample into silica-rich and silica-poor systems by establishing thresholds in the $S_{10,s}$ index. In our dichotomous terminology, a silica-rich system is characterized by observed features that closely resemble those of silica dust in sufficient abundance, exceeding the typical values found in circumstellar disks. The exact percentage of silica-rich PPDs is uncertain (largely because they were not the focus of early studies) but is likely under 10%, suggesting that advanced thermal processing in EDDs primarily drives the formation of silica dust.

A final characteristic commonly found in EDDs is that they often exhibit stochastic infrared variability on both short- (weekly to monthly) and long-term (yearly) timescales due to significant changes in the distribution of circumstellar dust. We quantified the disk variability using both decade-long WISE data at 3–5 μm (Appendix C.1) and 10/20 μm photometric data (Appendix C.2), where the WISE data probe the hotter part of the debris, while the 10/20 μm photometry traces both the 10 μm features resulting from small grains and warm dust particles. We found no strong correlation between infrared variability and dust content—measured as the infrared fractional luminosity—nor with stellar age and multiplicity (Figure C2), noting that only three EDDs in the sample are older than 300 Myr, and nearly all EDDs have companions at close, intermediate, and wide separations (Table A2). Surprisingly, the silica richness or poorness of the system does not impact the degree of variation; a mixture of behaviors, including fading, brightening, or both, is observed. Comparisons between the synthetic photometry derived from JWST spectra (obtained in 2023/2024) and other mid-infrared photometry from 1983–2022 indicate that fading behaviors are more frequently detected within the sample. Additionally, no significant morphological change is observed in the 10 μm feature, suggesting that the changes are primarily due to the amounts of dust rather than changes in dust composition. Overall, these findings indicate that the EDD dust mineralogy was inherited from the initial events that created the EDD phenomenon and has remained stable since its formation. The observed disk variability is linked to the aftermath of a past event, which may be the initial violent collision or subsequent related events triggered by that collision.

EDDs provide crucial insights into terrestrial-planet formation and subsequent evolution, particularly following the initial phase of giant planet formation in a gas-rich environment. The highly processed material, in the form of crystalline silicates and silica dust, offers diagnostic information about the physical conditions of giant impact events during terrestrial-planet formation, aiding in differentiating the complex outcomes of these impacts. We propose that silica dust in EDDs forms through gas-phase condensation during violent energetic events that experience greater shock levels than those primarily responsible for forming crystalline silicates, where both direct condensation and the annealing of existing dust play significant roles. As a result, silica-rich EDDs arise from collisions between planetary embryos, similar to the Mars-sized objects modeled in impact simulations, while silica-poor EDDs originate from collisions between smaller objects (i.e., Moon-sized objects) and/or less energetic impacts, such as low-velocity grazing events. Our hypothesis is well supported by impact simulations, which indicate that giant impacts involving planetary-embryo-sized objects generate less dispersible debris, as a significant portion is eventually accreted back to the emerging body. This finding aligns with observations that silica-rich systems exhibit relatively lower W_{10} values compared to their silica-poor counterparts. Additionally, we find that the prevalence of silica-rich EDDs peaks at a few hundred million years and diminishes after 300 Myr, providing robust observational evidence for the frequency of giant impacts among planet-sized bodies, and signaling the final phase of terrestrial-planet formation, as envisioned by theoretical simulations.

While no clear correlation exists between the EDD dust mineralogy (silica-rich versus silica-poor) and infrared variability at 3–5 μm, our analysis identifies a potential trend when differentiating EDDs by the amount of feature-producing small grains (i.e., W_{10}). The dynamical state of a planetary system, as measured by infrared variability, is 5 times higher for EDDs with large W_{10} (roughly one-third of the sample) than for those with small W_{10}, with all large W_{10} systems being exclusively silica-poor. The correlation between high-W_{10} values and the high degree of variability indicates that these silica-poor, large W_{10} systems are undergoing significant collisional activities, likely due to orbital instability caused by the dynamical interactions of unseen planets. This is further supported by the fact that three out of seven of these highly active, silica-poor EDDs are older than 300 Myr, beyond the expected epoch of terrestrial-planet formation. It is noteworthy that the emergence of these silica-poor, large W_{10} systems occurs around $\sim$100 Myr, although our sample is small. This leads us to propose that silica-poor EDDs with large W_{10} values might be signposts for planetary systems undergoing significant planetary rearrangement—for example, a phenomenon known as "breaking the chain," which has been identified to explain the architectural arrangement of mature multiple-planet systems. Our reasoning is threefold. First, no silica-rich EDDs have been found beyond the era of terrestrial formation ($>$300 Myr). Second, silica-poor EDDs likely result from collisions between Moon-sized bodies or less energetic events that produce minimal vapor condensates. The presence of large W_{10} values necessitates numerous such collisions, leading to increased dynamical activity, as indicated by infrared variability. Finally, both observational evidence and theoretical studies suggest that the phase of orbital instability that reshapes planetary architecture likely occurs within a few hundred million years. Our results, therefore, serve to motivate

future theoretical investigations aimed at linking "breaking-the-chain" models with observable dust production, a topic that has received little attention to date.

While our study provides observational evidence that enhances the characterization and definition of a subclass of DDs, the EDDs, and their connections to terrestrial-planet formation as well as systems experiencing orbital instabilities, many unexplored areas remain related to their direct relationships with these active research fields. Although impact simulations align with our general conclusions, many details need further investigation. For example, most simulations do not directly compute the vapor population because they lack or simplify shocked thermodynamic physics. How vapor condenses to dust (composition and size distribution), how composition is altered by melting, and how the resulting material subsequently evolves are important, because these processes directly determine the solid-state features observed in EDDs over time. Most EDDs are known to exist within binary or multiple systems; however, the absence of detailed information about companion stars—such as their mass and orbital properties—limits our ability to draw conclusive insights into their roles in the EDD phenomenon. This challenge is further compounded by the scarce information on other EDD properties, including the presence of existing planets and the cold components of distant planetesimal populations. Additionally, the small sample size (fewer than two dozen) significantly restricts our capacity to draw comprehensive conclusions. Expanding the sample to target specific parameter spaces and providing detailed characterization of known individual systems will further test the proposed connections.

Acknowledgments

Work on this paper was supported by grants 80NSSC24K1571 under the NASA ADAP program, and JWST PID 3189 program to the Space Science Institute, and partially supported by 80NSSC18K0555 from NASA Goddard Space Flight Center to the University of Arizona. A.M. is supported by the Hungarian National Research, Development and Innovation Office Élvonal grant KKP-143986. A.K. is supported by the NKFIH NKKP grant ADVANCED 149943. Project No. 149943 has been implemented with the support provided by the Ministry of Culture and Innovation of Hungary from the National Research, Development and Innovation Fund, financed under the NKKP ADVANCED funding scheme. A.A.S. is supported by the Heising-Simons Foundation through a 51 Pegasi b Fellowship. R.M. and I.P. acknowledge partial support from the National Aeronautics and Space Administration under agreement No. 80NSSC21K0593 program "Alien Earths." A.P.J. acknowledges support from the Towson University Fisher College of Science and Mathematics through the Fisher Endowed Chair of physical and biological sciences.

This research has made use of the NASA/IPAC Infrared Science Archive, which is funded by the National Aeronautics and Space Administration and operated by the California Institute of Technology.

K.Y.L. thanks Scott Kenyon for suggestions on editorial clarity and Chiyoe Koike for providing the laboratory measurements of silica.

The data presented in this article were obtained from the Mikulski Archive for Space Telescopes (MAST) at the Space Telescope Science Institute. These observations are associated with JWST programs 1206, 1282, and 3189. The standard pipeline-processed products can be accessed via DOI: 10.17909/14qb-nm35.

Facilities: JWST (MIRI), Spitzer (IRS), WISE.

Appendix A
Extreme Debris Disk Sample

Although dozens of EDD candidates have been identified using the all-sky WISE and Gaia catalogs (e.g., G. Contardo & D. W. Hogg 2024), the EDD nature of the 21 systems presented here has been confirmed by additional follow-up observations that determined their stellar properties and ruled out background contamination as false identifications of infrared excess. In particular, these systems all show indications of prominent 10 μm features, either from previous mid-infrared spectroscopy (mainly Spitzer/IRS) or narrow-band photometry (VLT/VISIR; A. Moór et al. 2024). Table A1 lists the JWST observations, including the program ID, observation date, and on-source exposure time. Table A2 gives other system properties, including those observed by Spitzer, and references used in this study. Most of the stellar properties, such as spectral type, temperature, mass, age, and multiplicity, were adopted from the literature when available, while we derive the values for those that are not. The uncertainties in the system age depend on the diagnostic methods (i.e., stellar lithium content, gyrochronology, magnetic activity, and kinematic properties); the listed values represent our evaluation of the literature values combined with our own assessments.

Table A2 also identifies the five EDDs for which cold ($\lesssim$150 K) dust is required either to fit their far-infrared spectral energy distributions (SEDs) or because their disk emission is resolved in the millimeter (analogous to the Kuiper Belt). Identifying a cold component typically requires far-infrared data, which many WISE-discovered EDDs lack. Consequently, whether a system hosts distinct (hot/warm/cold) planetesimal belts cannot be reliably determined from the SED alone (G. M. Kennedy & M. C. Wyatt 2014). We list this cold-component information only for completeness and for use in future individual studies. HD 166191, HD 113766, and RZPsc have Atacama Large Millimeter/submillimeter Array (ALMA) millimeter observations that detect dust emission confined within tens of astronomical units (K. Y. L. Su et al. 2023; L. Matrà et al. 2025; K. Worthen et al. 2026). HD 172555 and HD 145263 also have ALMA detections—the former is resolved as a compact disk ($<$10 au; Z. Roumeliotis et al. 2026) and the latter is unresolved (J. Lieman-Sifry et al. 2016). Importantly, their millimeter fluxes are consistent with the bulk SED emission at temperatures of $\sim$300–400 K, not with the cold dust typically inferred for Kuiper Belt analogs.

Multiplicity has also been found to be a common feature in EDDs, as suggested by previous studies (B. Zuckerman 2015; A. Moór et al. 2021, 2024). Excluding EDDs that are farther than 250 pc and less-studied systems, most EDDs have one or more companions at either very close (within a few astronomical units), intermediate (a few tens of astronomical units to 500 au), or wide ($>$500 au) separations (Table A2). Table A3 details the companions' properties collected from the literature for completeness and, like the cold-component information, serves as motivation for future detailed study.

Table A1
JWST Observation Log

ALLWISE ID	Short Name	PID	Obs. Date	BMJD	Exp[a]	References
J104416.70-451613.9	J1044	3189	2024-06-05	60466.495	888	(1)
J181030.32-233400.5	HD 166191	3189	2024-05-04	60434.184	99	(2), (3)
J061103.54-471129.2	J0611	3189	2024-04-01	60401.107	222	(4)
J010942.07+275701.7	RZPsc	3189	2024-07-28	60520.001	222	(5)
J060513.59-191308.4	J0605	3189	2024-03-06	60375.608	444	(4)
J060917.00-150808.5	J0609	3189	2024-03-06	60375.567	222	(1)
J204315.23+104335.3	J2043	3189	2024-06-22	60483.087	444	(1)
J092521.90-673224.8	J0925	3189	2024-05-07	60437.758	222	(1)
J230112.67-585821.9	J2301	3189	2024-08-16	60538.662	888	(6)
J121334.13-053543.4	J1213	3189	2024-06-22	60483.332	888	(4)
J071206.54-475242.3	J0712	3189	2024-03-16	60385.209	888	(1)
J080902.49-485817.2	ID8	1206	2024-01-07	60316.715	888	(7)
J032818.69+483947.9	V488Per	1206	2024-02-25	60365.240	177	(8)
J034638.40+225510.7	HD 23514	1206	2023-09-23	60210.761	133	(9), (10)
J023050.76+553253.3	HD 15407	1206	2023-09-23	60210.808	111	(11)
J184526.93-645218.1	HD 172555	1282	2023-09-18	60205.475	654	(12), (13)

Notes.
[a] On-source exposure time per subband per channel.
Reference: (1) A. Moór et al. 2024, (2) G. M. Kennedy et al. 2014, (3) K. Y. L. Su et al. 2022, (4) A. Moór et al. 2021, (5) K. Y. L. Su et al. 2023, (6) C. Melis et al. 2021, (7) K. Y. L. Su et al. 2019, (8) G. H. Rieke et al. 2021, (9) J. H. Rhee et al. 2008, (10) K. Y. L. Su et al. 2025, (11) H. Fujiwara et al. 2012, (12) C. M. Lisse et al. 2009, (13) M. Samland et al. 2025.

Table A2
EDD Properties

Name	D (pc)	SpT	T_* (K)	M_* ($M_\odot$)	L_* ($L_\odot$)	Age (Myr)	Multip.	Close	Intermediate	Wide	Silica Rich	Cold Comp.	Large W_{10}
HD 166191	100.8	G0V	6000	1.6	4.10	10	✓	…	✓[a]	✓	✓	✓	…
EFCha	104.5	A9IV	7500	1.5	2.77	10	✓	…	✓	…	…	…	…
HD 113766	122.5	F5V	5520	1.5	7.00	15	✓	…	✓	…	…	✓	…
HD 145263	141.9	F2V	6500	1.6	4.12	15	…	…	…	…	✓	…	…
HD 172555	28.3	A7V	8000	1.8	8.70	20	✓	…	…	✓	✓	…	…
RZPsc	184.7	G8V	5500	1.1	0.80	30	✓	…	✓	…	…	✓	…
ID8	358.7	G6V	5500	0.9	0.72	35	…	…	…	…	…	…	✓
V488Per	173.5	K0V	4760	0.8	0.31	80	✓?	…	…	✓	✓	✓	…
P1121	459.2	F9V	5750	1.1	1.50	80	…	…	…	…	…	…	✓
J0925	98.9	K4.5V	4510	0.6	0.22	85	✓?	…	…	…	…	✓	…
J0605	262.1	G5V	5660	1.0	0.94	120	×	…	…	…	…	…	✓
J0611	184.1	G9V	5350	0.9	0.65	130	✓	…	…	✓	✓	…	…
J1213	242.1	F6V	6350	1.2	2.55	>150	✓	…	…	✓	✓	…	…
HD 23514	139.1	F5V	6500	1.3	3.00	150	✓	…	✓	…	✓	…	…
HD 15407	49.3	F5V	6750	1.3	3.60	150	✓	…	…	✓	✓	…	…
J0609	348.3	G9V	5410	0.9	0.49	208	✓	…	…	✓	…	…	…
J0712	174.3	K3.5V	4680	0.7	0.28	243	✓?	…	…	…	…	…	✓
J2043	117.5	K4V	4640	0.7	0.21	252	✓	…	…	✓	…	…	…
J2301	158.1	G9V	5300	0.9	0.65	600	✓	…	…	✓	…	…	✓
BD+20307	117.3	G0V	5540	1.0	3.00	1000	✓	✓	…	✓	…	…	✓
J1044	199.1	K0.5V	5240	0.8	0.41	5500	✓	…	…	✓	…	…	✓

Notes. Symbols ✓ for yes and × for no in stellar multiplicity with companions in three different separations: close (<a few astronomical units), intermediate (a few tens of astronomical units to 500 au), and wide (>500 au). The "?" symbol means the presence of companions is inferred from Gaia astrometry. "..." means systems are too far to have useful constraints on stellar multiplicity. Large W_{10} systems are the ones with values >12.5 μm.
[a] There are two close ($\sim 1''$), faint sources around HD 166191 reported by A. Schneider et al. (2013), and one has been found comoving with the star (private communication).

Similarly, no planetary objects have been reported as associated with these systems. These stellar properties (age, luminosity, and multiplicity) are further used to search for correlations with the derived properties of the EDDs (see Appendix C for details).

The mid-infrared disk spectra shown in Figure 1 were derived by subtracting the stellar contribution using Kurucz atmospheric models estimated by the stellar type, temperature, and distance. We note that the MIRI/MRS spectra of

Table A3
Companion Properties

Companion for Target	SpT	M_* ($M_\odot$)	Separations (arcsec)	Separations (au)	e	e^{dn}	e^{up}	References
HD 113766	F6V	⋯	1.39	151.4	0.50	0.37	0.85	(1), (5)
HD 172555	K5Ve	⋯	71.34	2054	⋯	⋯	⋯	(13)
RZPsc	mid-M	0.12	0.13	23.0	⋯	⋯	⋯	(2)
V488Per	⋯	⋯	71.00	12277	⋯	⋯	⋯	(3)
J0611	M5.5	0.096 ± 0.01	24.64	4535	⋯	⋯	⋯	(4)
J1213	M4.5	0.19	4.17	1010	0.99	0.72	1.00	(4), (5)
HD 23514	M7	0.06 ± 0.01	2.65	368	⋯	⋯	⋯	(6)
HD 15407	K2.5	⋯	21.27	1048	0.63	0.33	0.86	(5), (7)
J0609	M4.5	⋯	1.96	682	⋯	⋯	⋯	(8)
J2043	M3.5	⋯	18.97	2228	0.64	0.43	0.87	(5), (8)
J2301	M4Ve	⋯	49.55	7836	⋯	⋯	⋯	(9)
BD+20307	WD	0.48–0.58	8.40	982	0.99	0.74	1.0	(5), (10), (11)
J1044	G8V	⋯	51.56	10266	0.99	0.76	1.0	(5), (8)
EFCha	⋯	⋯	1.44	147.6	0.96	0.63	1.0	(5), (12)

Note. Companion properties—spectral type (SpT), mass (M_*), projected separation, and eccentricity (e) with lower and upper bounds (e^{dn} and e^{up}) were collected from references: (1) C. H. Chen et al. 2011, (2) G. M. Kennedy et al. 2020, (3) B. Zuckerman 2015, (4) A. Moór et al. 2021, (5) H.-C. Hwang et al. 2022, (6) D. R. Rodriguez et al. 2012, (7) C. Melis et al. 2010, (8) A. Moór et al. 2024, (9) C. Melis et al. 2021, (10) (Z. D. Hartman & S. Lépine 2020), (11) N. P. Gentile Fusillo et al. 2019, (12) C. Briceño & A. Tokovinin 2017, (13) F. J. Alonso-Floriano et al. 2015.

HD 172555 and HD 23514 have been published previously by M. Samland et al. (2025) and K. Y. L. Su et al. (2025). Additionally, both ID 8 and V488Per have multiple epochs of MIRI/MRS spectra, but we only use the most recent ones for this work. We derived the infrared fractional luminosity (f_d) as listed in Table 1 by including the contributions of the prominent dust features, which provide a more accurate estimate than the previous values commonly derived from broadband photometry.

Although our mineralogy analysis solely focuses on the 10 μm region, all EDDs exhibit solid-state features in the associated 20 μm range, which is important for identifying the exact mineral composition and the Mg/Fe ratio in crystalline silicates (B. L. de Vries et al. 2018). Detailed spectral decomposition is needed to extract this information (e.g., A. Juhász et al. 2009; J. Olofsson et al. 2010), which is beyond the scope of the current work. We also note that a handful of the systems display noticeable features that are not characterized in the current study. Both HD 166191 and V488Per show a 6.3 μm feature arising from complex hydrocarbons (also called polycyclic aromatic hydrocarbons, PAHs) (P. A. Jensen et al. 2022) that are first detected in DD systems (Figure 1). Infrared gas emission lines have been reported in HD 172555 and HD 23514 (M. Samland et al. 2025; K. Y. L. Su et al. 2025), and here we report hot CO gas emission is also detected in HD 15407 for the first time. Additionally, CO_2 gas absorption features near 15 μm were also detected in HD 166191, RZPsc, and J0611, with the former two systems known to host highly inclined disks as shown through resolved imaging (K. Y. L. Su et al. 2023; K. Worthen et al. 2026), and cold CO emission has been detected in HD 166191 by ALMA (K. Worthen et al. 2026). A detailed analysis of these gas properties in EDDs will be reported in a future paper.

Appendix B
Dust Emissivity and 10 μm Dust Indices

B.1. Pseudocontinuum Estimate and Dust Emissivity

Under optically thin conditions, dust emission equals the dust opacity (which depends on composition and grain size) multiplied by the Plank function integrated over the emitting temperatures. Opacities are measured in the laboratory for a limited range of grain sizes and compositions or computed with theoretical models that rely on imperfect assumptions. Detailed spectral-decomposition studies using Spitzer data have sometimes reached discrepant conclusions owing to differences in adopted opacities or in dust temperature distribution arising from different disk structures (e.g., A. Juhász et al. 2009). With the new JWST spectra of EDDs, we revisit the reported mineralogical dichotomy (silica-rich versus forsterite-rich) reported in earlier Spitzer studies (e.g., H. Y. A. Meng et al. 2015). Rather than attempting definitive mineral identifications, we adopt a "dust emissivity" approach to robustly identify systems showing silica-rich signatures in the 10 μm region.

The dust emissivity (W_λ) is defined as the ratio between the feature-producing spectrum and the underlying continuum, i.e., $W_\lambda = (F_\lambda - F_{\lambda,c}) / F_{\lambda,c}$, where F_λ is the observed spectrum, and $F_{\lambda,c}$ is the continuum. Solid-state features arise from vibrational motions (stretching, bending, lattice modes) of atoms, ions, or molecules in a solid's fixed—ordered or partially ordered—structure; they are stronger for small particles and, therefore, are more useful to infer chemical composition. The purpose of defining a continuum is to separate emission from small grains, which produce prominent solid-state features, from emission by large grains so those features may be used to constrain composition. If all grains

share the same temperature distribution, dividing the observed spectrum by the Planck function integrated over that temperature profile (single, two-component, or more complex) largely isolates the small-grain emission. In practice, this separation is imperfect: small grains contribute a low-level smooth continuum in addition to discrete features, and some compositions (e.g., amorphous carbon) produce no distinct—or only very broad—features. Furthermore, it is unlikely all grains share the same temperature profile. For this reason, the continuum is termed a "pseudocontinuum" (D. E. Harker et al. 2023): it is not a true continuum but is useful for largely removing the temperature dependence.

Although silicate-like materials produce features in both the 10 and 20 μm regimes, these wavelengths often probe different disk regions in PPDs: the 10 μm feature is sensitive to dust in the inner au, while the 20 μm feature traces material at tens to hundreds of au from the star (e.g., H. Jang et al. 2024a, and references therein). This is consistent with early Spitzer studies showing that a two-temperature combination satisfactorily reproduces the mid-infrared silicate features arising from the optically thin regions of PPDs (J. Bouwman et al. 2008; B. A. Sargent et al. 2009a, 2009b; J. Olofsson et al. 2010). A power-law temperature distribution (e.g., A. Juhász et al. 2010), which is effectively similar to the polynomial approximation used by D. M. Watson et al. (2009) in PPDs, is also a valid alternative. We adopt both functional forms to determine the dust emissivity and assess the uncertainty introduced by the choice of functional form.

The anchor points used to define the pseudocontinuum also affect the derived dust emissivity. Ideally, they should lie in regions free of solid-state features; in practice, this is difficult—especially near 20 μm, where the amorphous-silicate feature is broad and essentially impossible to avoid within the limited wavelength range covered by JWST/MIRI. Consequently, we use second- or third-order polynomials rather than the fifth-order function used for fitting the Spitzer data by D. M. Watson et al. (2009). The pseudocontinuum is anchored to the disk spectrum at 5.6–7.0, 13.02–13.50, 14.32–14.83, and 24.5–26.0 μm with equal weighting; however, we reduce the weights of the last two anchors for systems with low levels of flat continuum from silica dust or with noisy data beyond 23 μm. The latter is particularly problematic for J0609, J2301, and V488Per, where the cooler temperatures used in the pseudocontinuum—derived from the limited wavelength coverage of JWST—are subject to large uncertainty. Among the 21 EDDs, the warm temperatures have a median of $\sim$750 K (range 350–900 K) and the cooler temperatures have a median of $\sim$225 K (range 100–300 K); the lowest warm temperature is found in HD 172555, while the lowest cooler temperature is found in V488Per and J0925. For the five EDDs observed with Spitzer IRS, a long-wavelength anchor between 35.07 and 35.92 μm, when available, was also used for pseudocontinuum determination. We stress that the two temperatures used for the pseudocontinuum span plausible extremes, with each having an independent normalization, and do not imply the disk consists of two narrow rings. Nonetheless, these temperatures indicate that (1) even if cold ($<$100 K) dust that emits prominently at 20 μm exists (we have no evidence for it given the derived temperatures), its contribution to the 10 μm region is insignificant, and (2) the 10 μm features predominantly originate from warm dust within a few astronomical units (i.e., the terrestrial zone).

As shown in Figure 1, the two pseudocontinua are very similar in the 10 μm region for most targets but can differ substantially in the 20 μm region. This is especially true for systems with large warm–cool temperature contrasts ($\sim$500 K), such as V488Per and J0925; without a reliable anchor for the cooler dust, the pseudocontinuum at 20 μm is highly uncertain. Solid-state features of crystalline silicates in the 15–25 μm region can aid mineral identification and help constrain the Fe/Mg ratio. However, feature strengths and profiles depend not only on Fe/Mg but are also highly sensitive to grain porosity and morphology, introducing significant degeneracies in compositional inferences (M. Min et al. 2007). For these reasons, we restrict our analysis to the 10 μm dust emissivity and defer in-depth spectral decomposition (including the 15–25 μm region) to future work.

B.2. Mathematical Forms

In this section, we define the properties of the 10 μm features used in this work and recap the mathematical forms of the dust indices from D. M. Watson et al. (2009), with the modifications described below. The feature's FWHM, equivalent width (W_{10}), and dust indices are measured from the derived dust emissivity, as shown in Figure B1: the FWHM and W_{10} probe the dominant small-grain sizes and the total mass of small grains, while the dust indices quantify the amount of thermally processed small grains in a system. We note that although FWHM is calculated assuming a Gaussian-like profile, real features are often non-Gaussian; FWHM can, therefore, be artificially small when a single sharp component dominates (e.g., the $\sim$9 μm silica peak in HD 172555). Increased crystallinity also broadens the 10 μm feature by extending its red and blue wings through contributions from crystalline olivine and pyroxene. Although we propose using W_{10} as a proxy for the dust mass of optically thin, small grains, this quantity is subject to several uncertainties. The pseudocontinuum anchoring ignores the low-level continuum contributed by small grains, causing a modest underestimation of true emission, and variations in grain-size distribution complicate mass comparisons across different systems. Consequently, these values should be treated with caution and used primarily for relative comparisons across a sample whose values are derived consistently.

We used the JWST MIRI/MRS spectrum of LkCa 15 as the "pristine-dust" reference, $W_{\lambda,0}$ near the peak wavelength $\lambda_R = 9.94$ μm (Figure B1), following the work of K. Y. L. Su et al. (2025). Note that the reference spectrum used in D. M. Watson et al. (2009) is a combined Spitzer spectrum of LkCa 15 and UY Tau; UY Tau was not observed with JWST. We will discuss the suitability of using LkCa 15 as the reference in Appendix B.3. The equivalent width and dust indices at 10 μm are calculated as integrals over a wavelength range $d\lambda$ as:

$$W_{10} = \int W_\lambda \, d\lambda,$$

$$X_{10} = \frac{\int_{\lambda_X-\Delta\lambda}^{\lambda_X+\Delta\lambda} W_\lambda \, d\lambda}{\int_{\lambda_R-\Delta\lambda}^{\lambda_R+\Delta\lambda} W_\lambda \, d\lambda} \frac{\int_{\lambda_R-\Delta\lambda}^{\lambda_R+\Delta\lambda} W_{\lambda,0} \, d\lambda}{\int_{\lambda_X-\Delta\lambda}^{\lambda_X+\Delta\lambda} W_{\lambda,0} \, d\lambda},$$

where $X = P$, O, and S for the peak wavelengths of crystalline pyroxene and olivine and silica, located at $\lambda_P = 9.21$ μm, $\lambda_O = 11.08$ μm, and $\lambda_S = 12.46$ μm. The procedure so far has

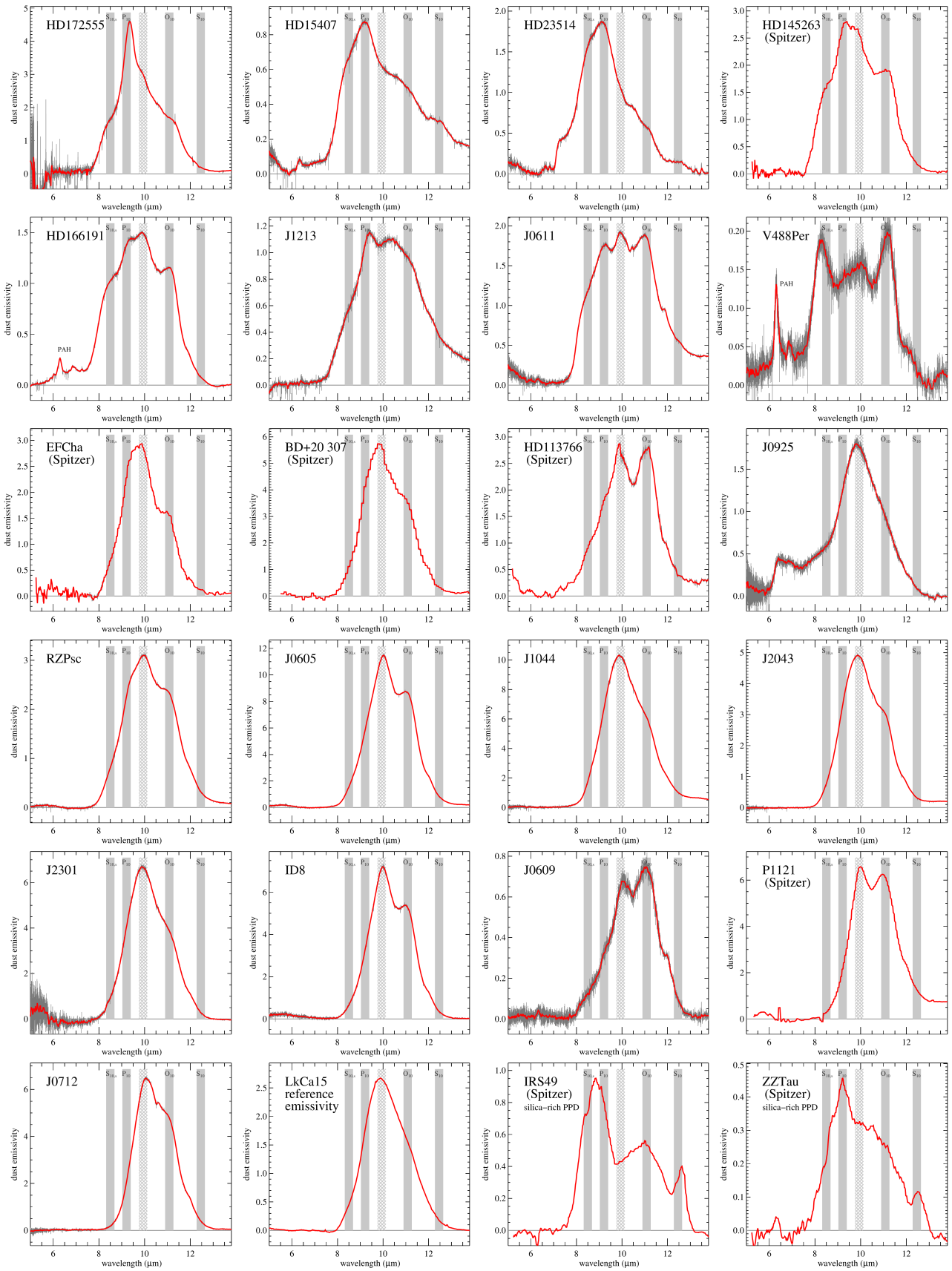

Figure B1. Dust emissivity of EDDs in the 10 μm region with the pseudocontinuum modeled as a combination of blackbodies. The top row shows the silica-rich system identified by Spitzer, while the second row shows the new silica-rich system identified by this work. The bottom row's last three panels show the reference emissivity from LkCa 15 and two silica-rich PPDs (IRS 49 and ZZ Tau). The vertical gray bars mark the wavelength regions for computing the dust indices (defining $S_{10,s}$, P_{10}, nominal 10 μm reference peak, O_{10}, and S_{10}; for details, see Appendix B.2).

followed the methodology from D. M. Watson et al. (2009), where the reasoning behind the choices is well documented. We added a new dust index, $S_{10,s}$, centered at $\lambda_{S_{10,s}} = 8.50$ μm, to better capture the blue side of the silica feature (C. Koike et al. 2013), and used both S_{10} and $S_{10,s}$ to characterize the silica dust. To minimize the overlapping wavelength between crystalline pyroxene and silica, we also reduced the integration range by a third compared to the value used by D. M. Watson et al. (2009), i.e., $\Delta\lambda = 0.182$ μm. For W_{10}, the integration was performed between 7.2 and 13.0 μm.

We initially estimated uncertainties in the derived 10 μm properties using a bootstrap: resampling the emissivity 500 times with propagated errors and taking the standard deviation of the resulting properties, following D. M. Watson et al. (2009). The bootstrap performs well when measurement noise dominates but yields very small uncertainties for high signal-to-noise (S/N) JWST spectra (typically <1%). Therefore, we adopt two different pseudocontinuum forms to quantify the systematic uncertainty in the derived 10 μm properties as given in Table 1. The differences are typically <1% for FWHM and <6% for W_{10}. Uncertainties are similar for systems with JWST- and Spitzer-derived emissivities, although Spitzer ones include additional anchor points beyond 30 μm. Typical uncertainties are 2% for both P_{10} and O_{10} (up to 5% in rare cases). For the silica indices, the typical uncertainty is 8% for both $S_{10,s}$ and S_{10} but exceeds 20% in rare cases.

To ensure that our modifications yield consistent results within uncertainties, we compare the indices calculated using both the old and new methods for 13 PPDs, where Spitzer IRS spectra are available in CASSIS (V. Lebouteiller et al. 2011), including the five silica-rich PPDs studied by B. A. Sargent et al. (2009a). For crystalline silicate indices (P_{10} and O_{10}), the maximum difference between the old and new definitions is 5%. For the silica index (S_{10}), the difference is 3 times larger, with the new values mostly being higher—likely because the narrower integration wavelength range increases the feature contrast. When plotting the old index values from D. M. Watson et al. (2009) on the new-index axes (e.g., Figure 3), differences for P_{10} and O_{10} are negligible, but S_{10} shows a noticeable upward offset (indicated by arrows). We note that the systematic offset between the new and old index definitions may affect exact, system-by-system comparisons, but the overall distribution (i.e., spread) remains unchanged for comparative studies. Additionally, we excluded PPDs with host masses $<0.5\,M_{\odot}$, yielding a sample of 34 PPDs from D. M. Watson et al. (2009) that matches the host-mass range of the EDDs for comparisons in Figure 3. For the new $S_{10,s}$ indices, in additional to the previous Spitzer PPD spectra, we also derived 10 μm dust properties for an additional 16 PPDs from archival JWST MIRI/MRS observations, all using a polynomial pseudocontinuum.

B.3. Dust Indices for Various Materials

The dust indices represent the contrast between the observed and pristine spectra. Specifically, the indices should be close to 1 if the two profiles are nearly identical, while a departure from that value indicates the prominence of a specific signature, assuming that the grain sizes are similar. To provide better perspective, we computed the 10 μm properties (peak, FWHM, and dust indices) for a wide variety of compositions, ranging from synthesized materials to theoretically calculated absorption coefficients. The results are listed in Table B1, with some shown in Figure B2. We particularly focus on the silica-like composition because different polymorphs of silica are formed under varying pressures and temperatures, making them valuable as a thermo-pressure gauge for their formation environment.

We first assess how similar the LkCa 15 10 μm emissivity is to ISM-like dust, the presumed source material for PPDs. Comparing this metric with actual observations and theoretical ISM opacities (dominated by ~submicron size) clarifies the composition effects and associated uncertainties. The observational reference is F. Kemper et al. (2004), who used ISO spectra toward the Galactic Center to derive the interstellar dust optical depth across the 10 μm region. We adopt the precomputed absorption coefficient for Mg-rich, 0.1 μm amorphous silicates from the `DuCKLing` package (T. Kaeufer et al. 2024), mimic the effect of pseudocontinuum anchoring, and compute the resulting emissivity both with and without the last point beyond 30 μm. Figure B3 compares the results with the LkCa 15 dust emissivity. The 10 μm profiles are very similar, while differences are larger in the 20 μm region, consistent with our earlier conclusion that the derived 20 μm emissivity is more uncertain. Although the profiles resemble each other, the computed dust indices are not exactly unity (see Table B1, which also lists three theoretical ISM opacities from M. Min et al. 2007), indicating subtle differences. We define an empirical boundary based on these ISM-like dust indices. Deviations from that boundary are unlikely to arise solely from pseudocontinuum removal or from the calculation method and instead most likely indicate an increased crystalline contribution (thermal processing), since ISM dust is known to have low crystallinity (F. Kemper et al. 2004; M. P. Li et al. 2007). M. Min et al. (2007) confirmed the absence or scarcity of crystalline silicates (and silica) in the ISM by fitting the observed 10 and 20 μm optical-depth profiles using three computational approaches that account for grain porosity. Their study also found interstellar silicates to be highly Mg-rich and to include a ~3% silicon-carbide (SiC) component, which broadens the overall 10 μm feature. For O_{10}, ISM dust spans 0.73–0.88, and for P_{10} it spans 1.17–1.50. Although the equivalent ranges for silica indices are broad—S_{10}: 1.19–2.57 and $S_{10,s}$: 0.98–2.61, likely reflecting compositional effects—these values remain below the lowest values measured for laboratory silica-rich materials. These comparisons suggest that LkCa 15's dust composition may differ slightly from the ISM—a difference also noted for the "pristine" composition of solar system comets (D. H. Wooden 2002). In practice, the precise definition of ISM-like dust composition is not critical, since the indices reflect relative measurements as long as the reference remains consistent. This is why we adopt LkCa 15 as the dust emissivity reference, allowing for the consistent integration of earlier studies with current work.

We use two other sources of laboratory materials to further validate the dust indices: processed materials (same initial composition subjected to different shock pressures) and synthesized materials with varied compositions. Processed materials are represented by mid-infrared spectra of carbonaceous chondrites (CM-type) experimentally shocked at different pressures, as measured by A. Morlok et al. (2010). CM chondrites are thought to be some of the most primitive materials in our solar system, having undergone minimal

Table B1
10 μm Properties for Dust Material

Sample Name	Peak (μm)	FWHM (μm)	P_{10}	O_{10}	S_{10}	$S_{10,s}$	Note
Silica-like composition							
Quartz	9.15	0.50	13.67	0.35	19.39	21.09	(1)
Fused Quartz	8.93	0.74	13.23	0.19	12.15	32.36	(1)
Cristobalite	9.09	0.51	10.61	0.49	14.25	20.57	(1)
Coesite	9.17	0.69	8.77	0.36	5.73	16.03	(1)
Stishovite	11.58	4.42	1.68	1.95	13.72	4.19	(1)
Mesosiderite	9.05	1.20	4.39	0.91	7.19	10.33	(2)
Obsidian	9.25	2.40	2.03	0.72	8.19	6.35	(2)
Shocked Shergott	9.35	3.00	1.51	1.31	4.08	2.98	(2)
SiO_2 Glass	9.00	1.55	9.94	0.98	14.11	30.65	(2)
Tektite A	9.20	3.85	1.88	1.09	6.08	6.21	(2)
Tektite B	9.25	3.20	1.84	1.05	3.90	5.43	(2)
Processed material							
Unshocked[a]	10.15	1.60	0.64	0.74	0.38	0.42	(3)
Medium Shock	9.95	2.00	0.72	0.95	0.55	0.53	(3)
Average Shock	10.05	2.30	0.77	1.40	0.91	0.68	(3)
High Shock	11.05	2.70	1.10	1.75	1.29	1.22	(3)
Maximum Shock	11.15	1.80	0.46	2.56	1.95	0.71	(3)
Synthesized material							
Forsterite	11.24	1.58	0.31	2.68	1.75	0.56	(4)
C. Enstatite	10.66	2.83	2.51	1.81	2.48	1.63	(5)
Diopside	9.28	2.56	2.77	1.90	2.02	1.16	(5)
Enstatite Gel	10.00	1.27	0.74	0.51	1.97	0.97	(5)
Diopside Glass	10.10	2.84	1.16	1.41	3.10	1.86	(5)
ISM-like composition							
Diff. ISM	9.75	2.00	1.18	0.84	...	0.98	(6)
Mg-rich silicates[b]	9.66	1.86	1.19	0.78	1.19	1.11	(8)
coatedGRF[b]	9.60	2.30	1.50	0.88	2.57	2.61	(7)
dhsfmax0p7[b]	9.55	2.15	1.49	0.84	2.20	2.60	(7)
porousGRF[b]	9.55	2.15	1.47	0.87	2.41	2.26	(7)
spherical[b]	9.55	1.95	1.45	0.73	1.52	1.93	(7)

Notes.
[a] CM-type carbonaceous chondrites (A. Morlok et al. 2010).
[b] Models of ISM composition with removal of narrow anchoring pseudocontinuum.
References: (1) C. Koike et al. 2013, (2) A. Morlok et al. 2014b, (3) A. Morlok et al. 2010, (4) C. Koike et al. 2003, (5) H. Chihara et al. 2002, (6) F. Kemper et al. 2004, (7) M. Min et al. 2007, (8) T. Kaeufer et al. 2024

alteration since their formation. As shown in Table B1, O_{10} dust indices are good tracers for experimental shock pressure; as the pressure increases, the forsterite peak becomes increasingly prominent. As discussed by A. Morlok et al. (2010), the strongly shock-melted sample (above 36 GPa) exhibits features of olivine that have recrystallized from melted material, closely resembling those found in the disks HD 113766 and HD 69830. Interestingly, while the indices for the maximally shocked material are similar to those of forsterite dust, they do not precisely match those of a pure synthesized forsterite sample. This further reinforces the idea that varying degrees of impurity in the material, along with the specific Mg/Fe ratio in the shocked, forsterite-rich material, influence the resulting indices. We also note that these melted, shocked forsterite-rich materials have silica indices well below those of silica-rich samples, making misidentification between the two unlikely.

Using dust indices from PPDs and previously analyzed EDDs/DDs (from spectral-decomposition studies), we perform a comparative mineralogical analysis emphasizing the degree of thermal processing. The index distribution in PPDs lies mostly outside the low-crystallinity ISM-like boundary. The ranges of indices in P_{10} and O_{10} reflect silicate crystallinity (the top row of Figure 3), varying from low (a few percent) to high (several tens of percent), calibrated from PPD studies (I. Oliveira et al. 2011). Similarly, EDDs (and DDs where small, warm grains are present) generally exhibit crystallinity levels comparable to those in PPDs. Two well-studied forsterite-rich debris systems, β Pic and HD 69830, showcase this association; high-quality Spitzer/IRS spectra indicate crystallinities of approximately 3% for β Pic (C. H. Chen et al. 2007) and 30%–40% for HD 69830 (J. Olofsson et al. 2012), aligning with their positions in the O_{10} index distribution. An additional consistency check comes from well-known forsterite-rich EDDs, where detailed dust mineralogy has been derived using Spitzer/IRS spectra. Both HD 113766 and BD+20307 exhibit high crystallinity ($\gtrsim$30%) (J. Olofsson et al. 2012). In the case of HD 113766, there is a

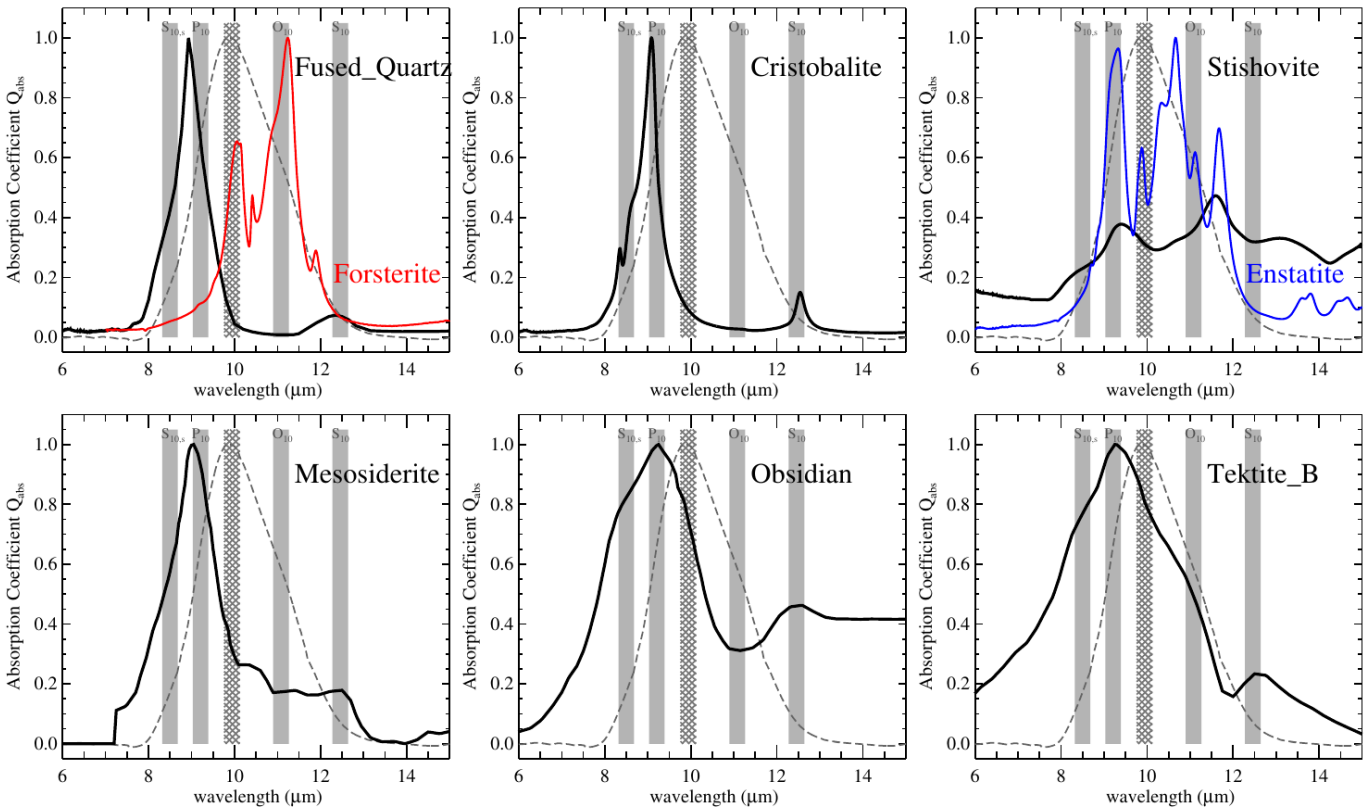

Figure B2. A sample of silica dust absorption coefficients (thick black lines, measured in the laboratory) in the 10 μm region compared to pristine, ISM-like dust emissivity (gray dashed line). The top row shows the synthesized, silica materials from C. Koike et al. (2013), along with synthesized forsterite (red, Mg-rich olivine) from C. Koike et al. (2003) and clinoenstatite (blue, Mg-rich pyroxene) from H. Chihara et al. (2002). The bottom row shows the three of the natural impact samples from A. Morlok et al. (2014b). The vertical gray bars mark the wavelength regions for computing the dust indices as in Figure B1.

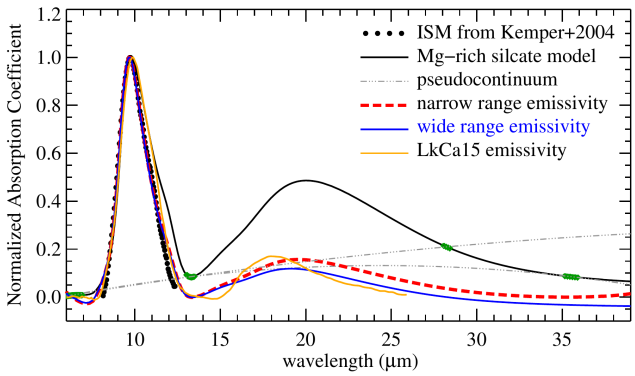

Figure B3. Comparison in the ISM-like dust emissivity. Dots: the observed absorption coefficient derived from the optical depth from F. Kemper et al. (2004). Orange line: the derived dust emissivity of LkCa 15 using the JWST spectrum. Blue solid and red dashed lines are the model dust emissivities computed from a model absorption coefficient for 0.1 μm, Mg-rich silicates (black) with two different pseudocontinua (narrow and wide anchoring ranges). The 10 μm profiles are all very similar (relatively insensitive to exact composition), while the 20 μm profiles are more uncertain.

greater contribution from forsterite (as traced by O_{10}) compared to enstatite (as traced by P_{10}), while BD+20307 shows roughly equal contributions from both minerals. This is consistent with the index values presented in Table 1.

All EDDs observed with JWST show clear departures from the "pristine" ISM-like profile represented by the LkCa 15, evident in both the disk spectra (Figure 1) and the 10 μm emissivity profiles (Figure B1) even without detailed spectral decomposition. Forsterite-rich systems are readily identified by a double-peaked 10 μm profile (at ∼10.05 and 11.23 μm) with some also showing Fe-rich, crystalline olivine peaks at ∼16.3, 19.5, and 24.0 μm (C. Koike et al. 2003), consistent with earlier spectral-decomposition results (J. Olofsson et al. 2012). Similar peaks appear in many JWST spectra as well, but with shifted peak positions or markedly different profiles, indicating a range of mineral mixtures. Compared with Spitzer-identified silica-rich EDDs (HD 172555, HD 23514, HD 15407, HD 145263), several JWST spectra also show peaks near ∼8.6, 9.1, 12.5, and 16.1 μm, indicative of silica-rich minerals (C. Koike et al. 2013). Although, some of these peaks are muted or less pronounced in certain sources. This reflects the fact that, in a real astronomical environment, dust is a mixture of many minerals, and the dominant composition can only be identified by comparing profiles dominated by different species. We perform this comparison using dust indices and by grouping systems with similar index values to identify minerals of interest, specifically silica.

As shown in Table B1, all nearly pure silica compositions prepared in the laboratory (∼submicron size) have peak wavelengths in the 10 μm region ranging from 8.93–9.25 μm, except for stishovite, which peaks at 11.58 μm. All silica-rich materials exhibit high S_{10} and $S_{10,s}$ indices: the lowest S_{10} is 3.90 (Tektite B) and the lowest $S_{10,s}$ is 2.98 (shocked shergottite). Most silica-rich samples also show high P_{10} but relatively low O_{10} values. We use the silica indices from previously identified silica-rich systems—four EDDs (HD 172555, HD 23514, HD 15407, and HD 145263 from Table 1) and six PPDs (Table B2) from B. A. Sargent et al. (2009a) and K. M. Pontoppidan et al. (2024)—to set thresholds

Table B2
10 μm Properties of Silica-rich PPDs

Name	Peak (μm)	FWHM (μm)	W_{10}	P_{10}	O_{10}	S_{10}	$S_{10,s}$	Origin
IRS 49	8.85	3.19	2.59	2.79	2.15	10.69	10.35	(1)
FZTau	11.04	5.16	0.91	1.62	2.09	10.76	6.61	(2)
1RXSJ1614	9.08	3.31	0.75	2.05	1.58	4.15	5.73	(1)
T51	9.15	3.02	4.00	1.96	1.50	2.34	4.97	(1)
ZZTau	9.22	2.73	1.21	2.02	1.35	4.61	4.12	(1)
ROXs 42C	9.15	2.66	1.81	1.98	1.50	2.41	3.86	(1)

Note. (1) Spitzer data from B. A. Sargent et al. (2009a), (2) JWST data from K. M. Pontoppidan et al. (2024).

for identifying silica-rich systems. All 10 of these silica-rich systems have $S_{10,s}$ values larger than the lowest $S_{10,s}$ measured for silica-like laboratory material,[11] but only six meet the S_{10} threshold (the four that do not are HD 172555, HD 145263, T 51, and ROXs 2C). This is not surprising, since the S_{10} index probes the less-pronounced silica feature,[12] which is therefore more susceptible to pseudocontinuum uncertainties. Note that the silica indices do not distinguish between crystalline and amorphous silica; a sharper 12.46 μm feature (e.g., cristobalite, a crystalline polymorph; see Figure B2) would increase the S_{10} value if present in sufficient abundance. In real environments, dust is expected to contain mixtures of materials —different polymorphs of silica (crystalline or amorphous) and other minerals with varying impurities and porosities— that likely reduce the contrast of the weaker S_{10} feature. To be consistent with previous identifications, we therefore use $S_{10,s} > 2.98$ as the threshold for identifying silica-rich systems. The newly identified silica-rich EDDs are V488Per, J0611, J1213, and HD 166191; together with the four previously identified silica-rich EDDs from Spitzer, eight of the 21 EDDs (38^{+11}_{-9}%) are silica-rich. The labels "silica-rich" and "silica-poor" are relative to the sample and chosen threshold; including or excluding edge cases near the boundary does not affect our overall conclusions. By analogy, our derived $S_{10,s}$ indices yield an apparent silica-rich fraction of 27^{+9}_{-6}% among PPDs (eight of 30),[13] but that sample includes many preselected silica-rich systems and, thus, likely overestimates the true fraction. Using the ~80 Class II PPDs analyzed by the Spitzer/IRS GTO team gives a more representative silica-rich PPD fraction of $\sim 6^{+4}_{-2}$% (B. A. Sargent et al. 2009a; D. M. Watson et al. 2009) using Spitzer data.

As discussed in the main text, while we adopt a dichotomous terminology to describe EDD dust mineralogy (silica-rich versus silica-poor), this does not imply that silica-rich systems lack crystalline silicates or that silica-poor systems contain no silica at all. The study by J. Olofsson et al. (2012) demonstrated that ~7% of the dust in HD 69830 originates from β-cristobalite (a form of silica), while the crystalline silicate features in BD +20307 are best fitted with equal amounts of forsterite and enstatite, both of which are classified as silica-poor systems in our framework. We also note that crystalline silicates from both

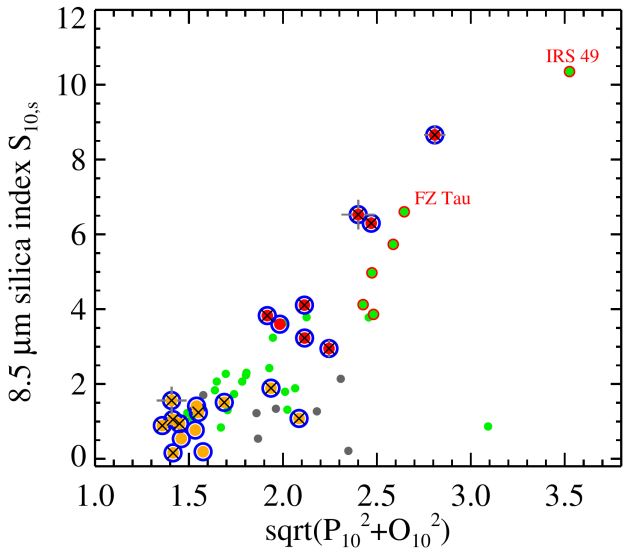

Figure B4. The distribution between the $S_{10,s}$ silica index and the combined crystalline silicate index ($\sqrt{P_{10}^2 + O_{10}^2}$), labeled as crystallinity. These indices suggest a positive correlation between the amounts of silica and crystalline silicates.

the olivine and pyroxene families are present in nearly all previously identified silica EDDs and PPDs. For silica-rich EDDs HD 172555 and HD 145263, 11% and 22% of the emission, respectively, are attributed to Mg-rich forsterite (C. M. Lisse et al. 2009, 2020), while crystalline silicates account for a few percent up to ~30% of the mass in the five silica-rich PPDs (B. A. Sargent et al. 2009a). Among the silica-poor systems, the last nine panels in Figure 1 show pronounced double peaks near 16 and 19 μm indicative of Fe-rich forsterite —which previously would have led to classification as forsterite-rich. Silica dust also has a feature at 16.1 μm, so determining whether the 16 μm feature in some silica-rich systems arises from a mixture with forsterite or from pure silica requires future detailed spectral decomposition.

To further explore potential trends between silica dust (represented by $S_{10,s}$ index) and crystallinity in EDDs, we derive a crystallinity measured by combining P_{10} and O_{10} as $\sqrt{P_{10}^2 + O_{10}^2}$. The results are illustrated in Figure B4. These indices suggest a positive correlation between the amounts of silica and crystallinity, indicating that silica-rich systems are more frequently found in environments with high crystallinity, including PPDs. The presence of a small amount of silica in HD 69830, combined with its high crystallinity, is consistent with the observed correlation, reinforcing that both silica and crystalline silicates are highly processed materials.

[11] HD 172555 has $S_{10,s} = 2.95 \pm 0.23$, which places it at the boundary of the lowest $S_{10,s}$ value within the errors.
[12] D. M. Watson et al. (2009) chose this wavelength, rather than the more prominent ~9 μm feature, to avoid confusion with the crystalline-pyroxene feature near ~9.21 μm when using a wider integration index.
[13] Two of the eight are newly identified silica-rich PPDs according to our criterion and were confirmed by J. Varga et al. (2026) using the spectral-decomposition technique; the other six were previously published shown in Table B2.

Appendix C
Infrared Variability

Infrared variability resulting from circumstellar material often serves as supporting evidence for identification as genuine EDDs. In light of the decommissioning of the NEOWISE mission, we have collected and documented all WISE W1 and W2 photometry from IPAC/IRSA and determined their variability behavior over the span of 15 yr, as detailed in Appendix C.1. In addition to the decade-long, regular 6 month sampling of disk variability using the WISE W1/W2 data, we further investigate the stability of the 10 μm feature by comparing the synthetic photometry derived from the JWST/MIRI/MRS spectrum to other existing 10–20 μm photometry as detailed in Appendix C.2.

C.1. 3–5 μm Infrared Variety as Traced by WISE W1/W2 Data

Following the analysis steps outlined in A. Moór et al. (2021), the W1/W2 measurements are calculated as an average of multiple single-exposure photometry taken every 6 months, and the disk contribution (i.e., excess flux) is obtained by subtracting the stellar contribution determined by atmospheric models (assuming a systematic uncertainty of 2%), which is assumed to be nonvariable. Although some optical variability is known to be associated with the host stars, the infrared variability is unlikely to arise from the star because the degree of infrared variability is often much larger than that coming from the stellar photosphere, particularly at longer wavelengths (i.e., 4.6 μm photometry is a better tracer for disk variability than 3.4 μm photometry). However, normalization of the stellar model does affect the resulting photospheric flux, particularly for systems with large interstellar extinction, which greatly influences the normalization using optical photometry. As a result, the disk flux becomes negative, especially during low disk flux states, such as for J2301 (see Figure C1).

The effect of stellar photospheric determination can be mitigated if we quantify the degree of variability in a relative sense by normalizing to a specific value. We used the minimum disk flux at 4.6 μm to represent the nominal background flux level maintained by collisions among existing small planetesimals, along with two indicators to quantify infrared variability: the maximum and typical (rms) variations, both expressed as percentages relative to the minimum disk flux at 4.6 μm. The typical variation reflects the stochastic nature of collisions, while the maximum variation captures the highest degree of change recorded in the data over the monitored period. Four out of the 21 EDDs are heavily saturated in W1/W2 photometry, making their single-exposure photometry unusable. HD 23514, HD 145263, and BD +20307 have single-exposure measurements that are partially affected by saturation. We employed the method described in the NEOWISE Explanatory Supplement[14] for saturation correction and found that the corrections are most significant at 3.4 μm for the latter two systems but not significant for HD 23514 or for the data at 4.6 μm. Furthermore, we validate the short brightening event observed in the 2022 data point of BD+20307 by examining the relevant single-exposure data of nearby stars. The final 16 disk light curves are presented in Figure C1. Four of the saturated systems have warm Spitzer time-series data that can be used to supplement the WISE data. Published results for HD 113766, HD 172555, and HD 166191 are sourced from K. Y. L. Su et al. (2020, 2022), while we find HD 15407 exhibiting stochastic variations of approximately 5%–10% using the archival data.[15]

We also computed the associated change in dust cross section, $\Delta\Sigma = \Delta F d^2/B_\nu(T_d)$, required to match the maximum flux change observed at 4.6 μm (ΔF) where d is the distance, and B_ν is the Planck function by assuming that (1) the emission is optically thin and (2) all dust is at the same temperature (T_d). Using the warmer temperature applied in the pseudocontinuum, we found that $\Delta\Sigma$ ranges from 1.85×10^{-4} au^2 to 1.60×10^{-2} au^2, with the largest values coming from V488Per and the smallest from J0712 (as illustrated in Figure C1). These values correspond to 2.7–233 times that of the stellar surface (assuming a size comparable to the Sun). We emphasize that these values are true minima due to the prior assumptions, suggesting that the variation originates from the circumstellar environment rather than from the star or the emerging planet itself (if any).

We compared the two variability percentage indicators (maximum and typical rms) and $\Delta\Sigma$ shown in the top two panels of Figure C2. The two variability percentage indicators are strongly correlated,[16] suggesting they are likely driven by a common physical process, such as the aftermath of a significant impact. Interestingly, there is no direct correspondence between the variability percentage (normalized to the minimum disk flux per system) and $\Delta\Sigma$, as illustrated in the upper-middle panel of Figure C2. While both quantities can be used to characterize the variable behaviors in EDDs, the former reflects the change normalized to the individual system, whereas the latter is anchored on an absolute scale, allowing for comparison among different stars. The uncertainty associated with both might be quite large in some cases due to the adopted assumptions, which transform the observed flux change to the variability levels. Both derivations assume that the observed flux change is solely due to changes in the emitting area, which is valid in the optically thin regime but should be treated as a lower limit otherwise. Additionally, $\Delta\Sigma$ has an additional assumption that the dust temperature is constant, which is unlikely to be the case.

We used both quantities to search for potential trends with other EDD properties, such as infrared fractional luminosity (f_d), age, 10 μm feature properties, and dust mineralogy. We note that EDDs are identified by large amounts of infrared excesses indicative of large amounts of circumstellar material with $f_d \gtrsim 10^{-2}$–10^{-3}. The only exception in our sample is HD 172555 with $f_d \sim 7 \times 10^{-4}$, whose classification is primarily based on its unique, silica-rich dust mineralogy (C. M. Lisse et al. 2009). We employed both Spearman and Kendall correlation coefficients, suited for smaller datasets, to search for the potential correlation among the derived properties with the p-values indicating the statistical significance of the results. The only pair of parameters with a potentially significant correlation is P_{10} and $\Delta\Sigma$. Even in this case, however, the p-values are only slightly lower than 0.05. Combined with the fact that our sample is small (there are only

[14] See https://irsa.ipac.caltech.edu/data/WISE/docs/release/NEOWISE/expsup/sec2_1civa.html.

[15] Adopted values for the variability analysis are: 200/10 for HD 166191, 15/5 for HD 113766, and 10/5 for both HD 172555 and HD 15407.

[16] To ensure that the correlation was not biased by the WISE cryogenic cooling effect, we also repeated the analysis using only NEOWISE data (after 2012), and the resulting correlation remained unchanged.

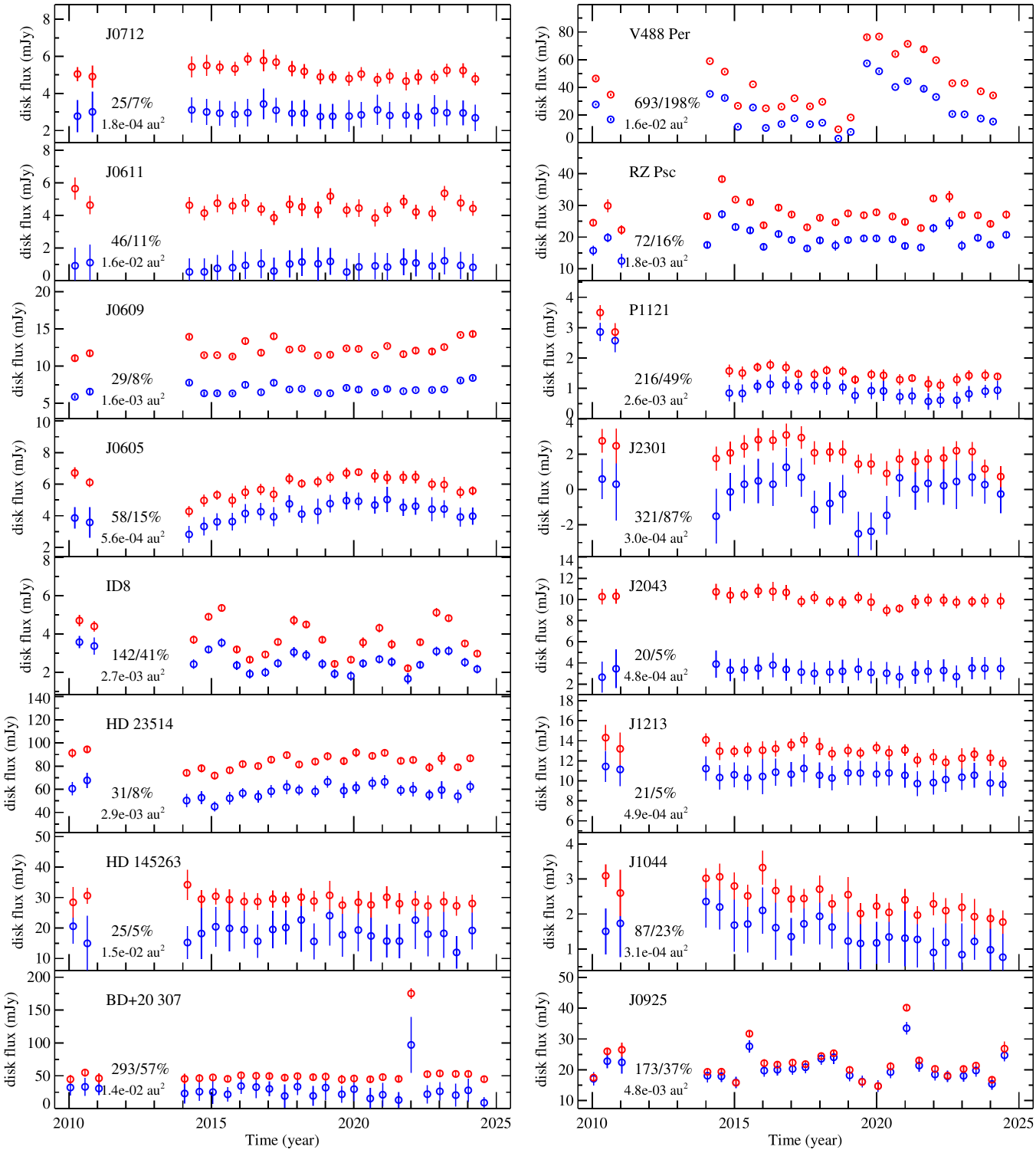

Figure C1. Each panel shows the individual WISE W1 (blue) and W2 (red) light curves. The maximum and typical variability percentages relative to the minimum disk flux at 4.6 μm are provided in each of the panel, along with the maximum change in the dust cross section in units of au^2.

three systems older than 300 Myr[17]) and the data are not normally distributed or contain outliers, these statistical tests reveal no strong correlations among the EDD properties.

The apparent lack of a strong correlation between the EDD properties and 3–5 μm variability is not surprising, as a system could remain in a quiescent state for extended periods before exhibiting large variations following a significant impact (K. Y. L. Su et al. 2022). Photometry at 3–5 μm only traces the hottest part of the disk. The varying time since the giant impact that created the EDD phenomenon for different systems further complicates the situation and prevents a clear correlation. The only potential trend related to disk variability emerges when we differentiate EDDs in W_{10} space, as illustrated in Figure 4.

[17] The age of 150 Myr for J1213 is a lower limit (A. Moór et al. 2021), and it could be older than 300 Myr given the uncertainty.

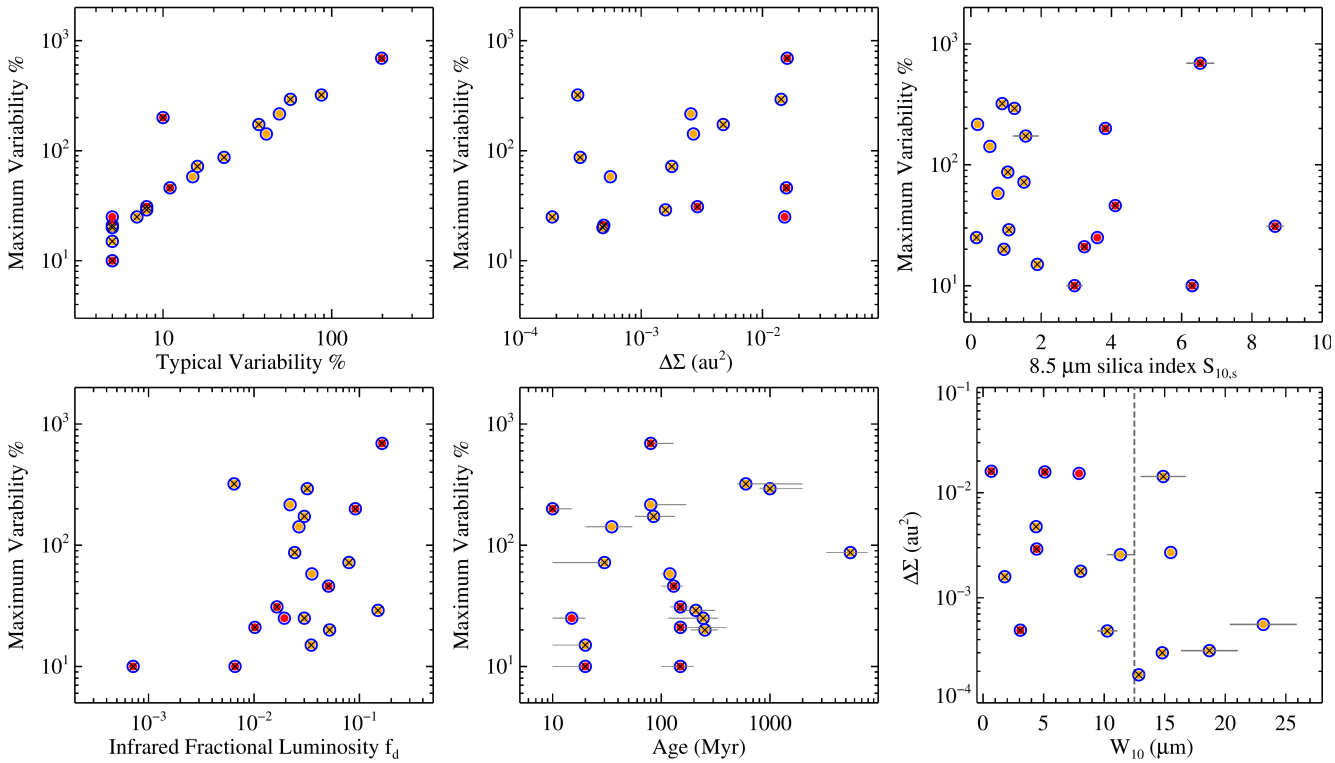

Figure C2. Relation between the observed 4.6 μm disk variability and selected EDD properties. The symbols and colors are the same as in the previous figures (red: silica-rich, orange: silica-poor, cross: multiplicity). The top-left panel displays a comparison between the two variability percentage indicators showing a tight correlation that suggests both track the aftermath of a significant impact. However, their relation to the change in dust cross section ($\Delta\Sigma$, on an absolute scale) is very weak, as illustrated in the upper-middle panel. The other panels show disk variability (using both the maximum variation percentage and $\Delta\Sigma$) vs. other EDD properties, such as silica indices $S_{10,s}$, infrared fractional luminosity (f_d), and age. None of these shows a strong correlation, including the derived dust mineralogy. The only potential trend is shown in Figure 4 with implications discussed in Section 4.

The median variability values for the large W_{10} ($\gtrsim$12.5 μm) systems, indicated by the horizontal dashed line, are $\sim$5 times higher than the median values for the small W_{10} systems. Notably, all large W_{10} systems are classified as silica-poor. However, such a difference is washed out in the $\Delta\Sigma$ space, likely due to variation in the dust location (i.e., temperature). The implications of these findings are discussed in Section 4.

We searched for possible correlations between multiplicity and EDD properties, and no obvious trends were found (some examples are shown in Figure C2). As noted by A. Moór et al. (2024), three of the old (>300 Myr) EDDs, which are now identified as having large W_{10} values, are all in wide binary systems with high eccentricity. However, not all EDDs with large W_{10} ($\gtrsim$12.5 μm) values have stellar companions (see Figure 4 and the lower-right panel of Figure C2). Given the small sample size, the exact role that multiplicity plays in creating EDD phenomenon is unclear. A larger sample, particularly one that extends to older ages, along with better determination of binary properties, is needed for future in-depth study.

C.2. 10/20 μm Variability as Traced by Synthesized Photometry

We further investigate the stability of the 10 μm feature by comparing the synthetic photometry derived from the JWST/MIRI/MRS spectrum to other existing 10–20 μm photometry from IRAS, AKARI, Spitzer, MSX, and ground-based mid-infrared instruments as outlined in N. Gorlova et al. (2007), A. Schneider et al. (2013), C. Melis et al. (2021), G. H. Rieke et al. (2021), A. Moór et al. (2021), and K. Y. L. Su et al. (2025). For the 16 EDDs observed with JWST, we assume a 2% uncertainty in the flux calibration, which is added quadratically when evaluating the significance of change (see Figure C3 for examples). As anticipated, we observe both brightening and fading behaviors as listed in Table 1. However, fading behavior is detected more frequently across the entire sample. Figure C4 displays the flux ratios between earlier and later JWST measurements for VLT/VISIR narrowband and WISE W3/W4 photometry. There are more systems with ratios >1 (indicating fading) than those with ratios <1 (indicating brightening). The robust average of the measured flux ratios (indicated by the horizontal line in Figure C4) is around 1, except for WISE/W4, which has a value of 1.12. Although the difference in absolute flux calibration might be a factor, it should affect all WISE bands, not just W4; therefore, we consider the general fading in WISE/W4 to be generic. This fading trend among the sample is expected if the EDD phenomenon is linked to the aftermath of a significant past event.

The consistent trend observed in the VLT/VISIR narrowband photometry for eight out of the 16 systems suggests that variability does not alter the overall shape of the 10 μm feature; instead, the changes are primarily attributed to the underlying continuum rather than the solid-state features from the small grains. While photometry alone is not definitive proof of this behavior, a similar conclusion was drawn from comparisons between JWST spectra and those from previous Spitzer or ground-based mid-infrared spectroscopic studies. Nearly identical dust features in the giant impact (silica-rich)

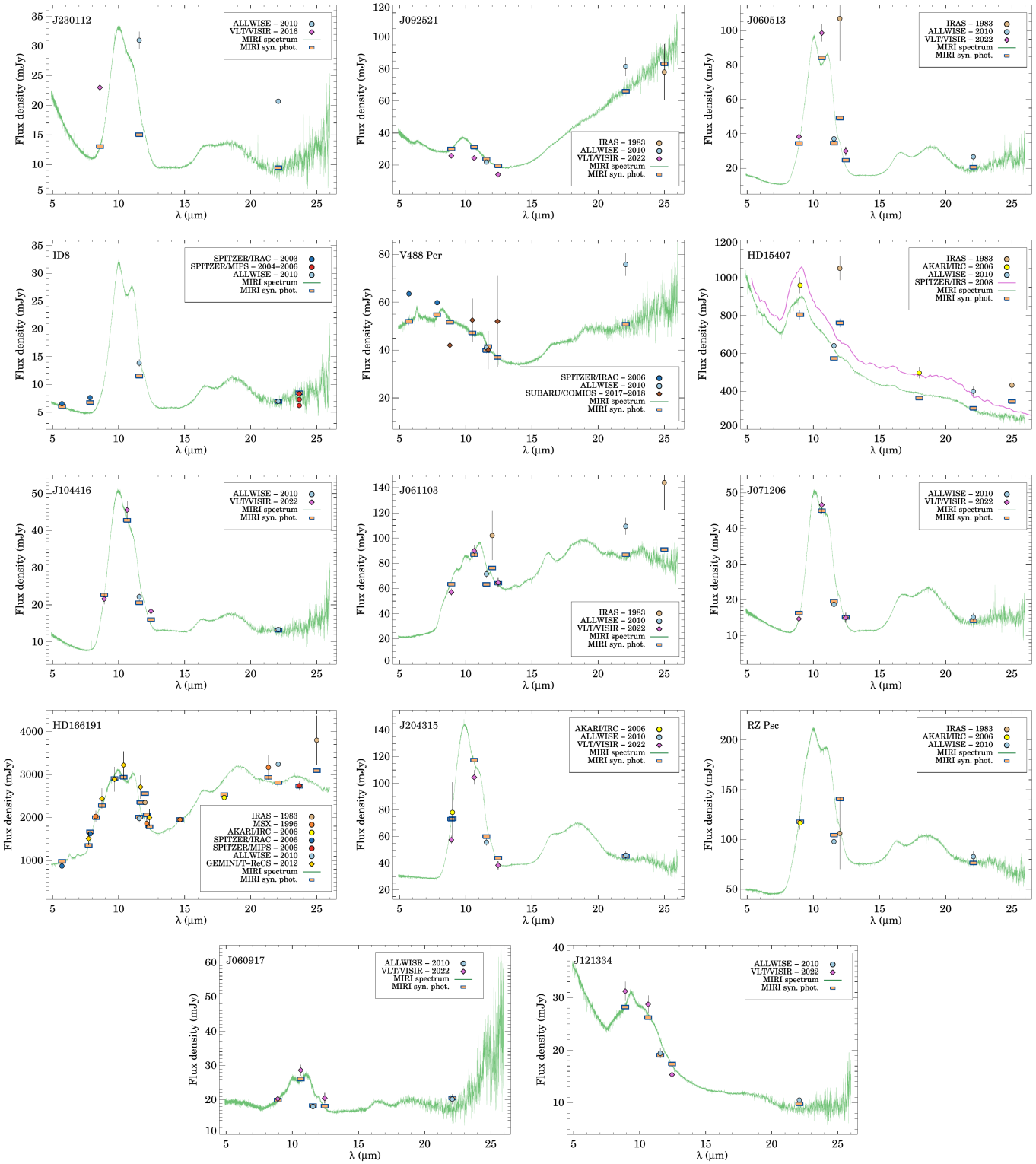

Figure C3. Mid-infrared 10/20 μm variability for 14 EDDs studied in this work by comparing previous photometry taken over the past few decades to the synthetic photometry derived from the 2024 JWST/MIRI/MRS spectra. The 10/20 μm variation behaviors are summarized in Table 1 along with other published studies (see K. Y. L. Su et al. 2025 for HD 23514 and M. Samland et al. 2025 for HD 172555). For HD 15407, the Spitzer/IRS spectrum taken in 2008 is also shown, illustrating the fading behavior along with similar solid-state features—commonly found in these EDDs—regardless of whether they exhibit fading, brightening, or both behaviors.

disks around HD 172555 and HD 23514 have been reported by M. Samland et al. (2025) and K. Y. L. Su et al. (2025), with the former exhibiting 5% brightening at 9 μm and the latter remaining stable at 9 μm but showing a 10% fading at 20 μm. Here, we report that the JWST spectrum of HD 15407, the third silica-rich EDD discovered by Spitzer, shows ∼15%–20% fading compared to the Spitzer one taken 15 yr earlier (Figure C3). The 10 μm properties derived from the Spitzer HD 15407 spectrum are:

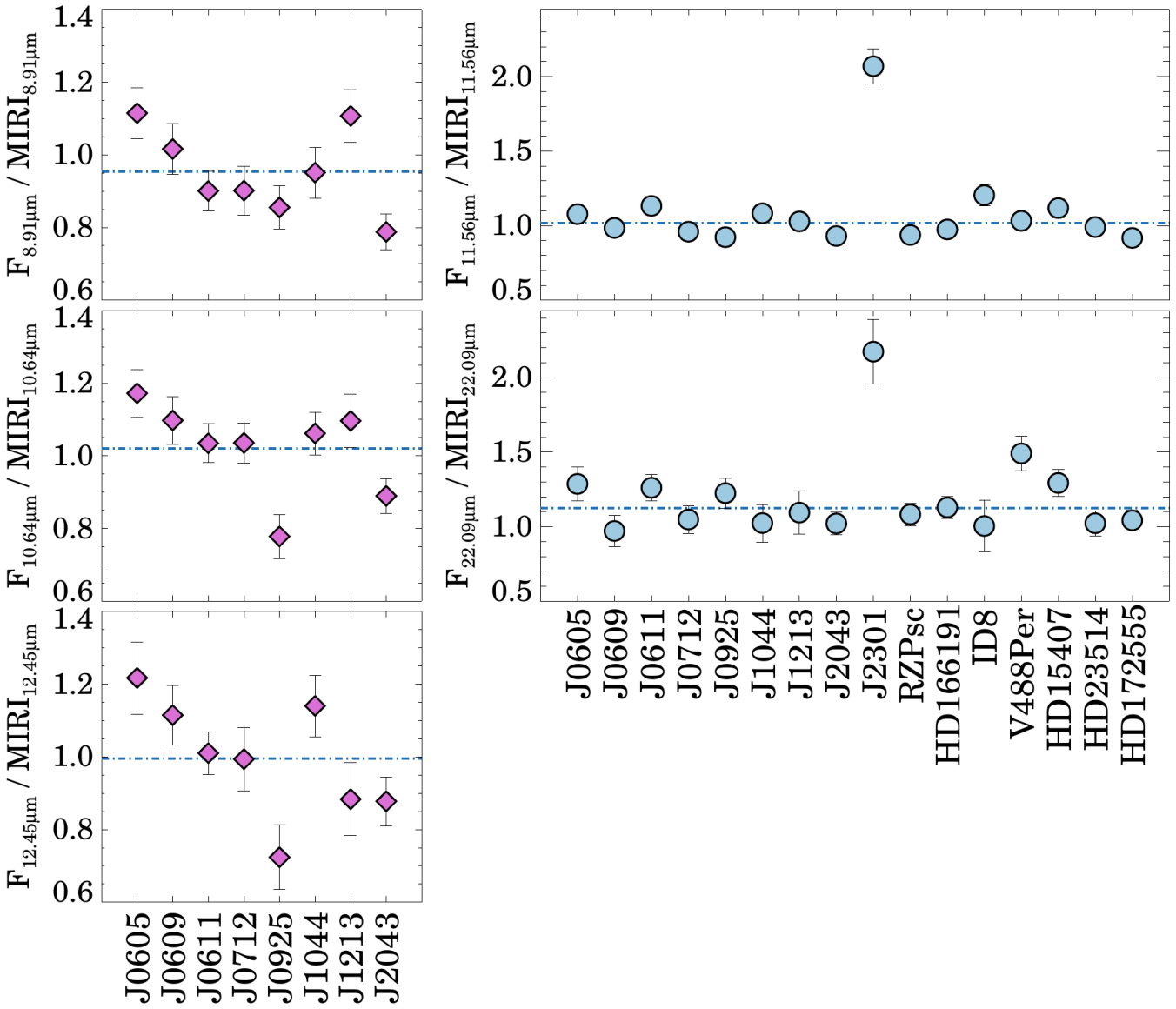

Figure C4. This figure shows the flux ratio between the previous 10/20 μm photometry and the synthetic values derived from the JWST/MIRI/MRS spectra. The left panel displays the results for the VLT/VISIR narrowband photometry, while the right panel depicts the results using WISE W3/W4 data

FWHM $= 3.15 \pm 0.12$, $W_{10} = 3.03 \pm 0.40$, $P_{10} = 2.04 \pm 0.06$, $O_{10} = 1.31 \pm 0.04$, $S_{10} = 7.62 \pm 0.69$, and $S_{10,s} = 6.08 \pm 0.17$—all very similar to the values from the JWST spectrum (Table 1), demonstrating the effectiveness of using dust indices. Additionally, both RZPsc and J2301 have VLT/VISIR *N*-band grism spectra (G. M. Kennedy et al. 2017; C. Melis et al. 2021) taken in 2016, and the feature morphology remains very similar to that of the JWST spectra taken in 2024. For J2301, although the dust composition as measured in the small grains remains stable, the W_{10} value drops by ~55% over a span of 8 yr (C. Melis et al. 2026, in preparation). V488Per, a silica-rich system identified in this study, has two epochs of JWST MIRI/MRS spectra taken 6 months apart that appear to be identical within calibration uncertainty. A silica-poor system, ID8, has four high-quality mid-infrared spectra including one from Spitzer/IRS, proving a baseline of 17 yr. All four spectra exhibit similar dust mineralogy (i.e., without changes in dust composition) but reveal varying degrees of wavelength-dependent variation in the dust continuum (K. Su et al. 2026, in preparation).

In summary, we found no clear correlation between the degree of disk variation and the impact-produced dust mineralogy or system age and multiplicity. Nonetheless, the EDD systems with a high level of optically thin dust (i.e., $W_{10} > 12$ μm) that are predominantly rich in forsterite dust tend to exhibit greater variability by a factor of 5, compared to the others. There appears to be no significant change in the 10 μm mineralogy, suggesting that the composition of small grains formed during past violent events remains unchanged over decadal timescales. The infrared variability in EDDs exhibits a wide range of behaviors, depending on the observed wavelengths, which may be different aspects of the impact-produced debris and reflect varying sampling times in the aftermath.

ORCID iDs

Kate Y. L. Su https://orcid.org/0000-0002-3532-5580
Attila Moór https://orcid.org/0009-0001-9360-2670
Ágnes Kóspál https://orcid.org/0000-0001-7157-6275
George H. Rieke https://orcid.org/0000-0003-2303-6519
Antranik A. Sefilian https://orcid.org/0000-0003-4623-1165
Renu Malhotra https://orcid.org/0000-0002-1226-3305
Ilaria Pascucci https://orcid.org/0000-0001-7962-1683
Alan P. Jackson https://orcid.org/0000-0003-4393-9520
Péter Ábrahám https://orcid.org/0000-0001-6015-646X
Nicholas P. Ballering https://orcid.org/0000-0002-4276-3730

References

Aannestad, P. A., & Purcell, E. M. 1973, ARA&A, 11, 309
Alibert, Y., Baraffe, I., Benz, W., et al. 2006, A&A, 455, L25
Alonso-Floriano, F. J., Caballero, J. A., Cortés-Contreras, M., Solano, E., & Montes, D. 2015, A&A, 583, A85
Armitage, P. J. 2024, arXiv:2412.11064
Asphaug, E. 2014, AREPS, 42, 551
Asphaug, E., & Reufer, A. 2013, Icar, 223, 544
Ballering, N. P., Rieke, G. H., & Gáspár, A. 2014, ApJ, 793, 57
Balog, Z., Kiss, L. L., Vinkó, J., et al. 2009, ApJ, 698, 1989
Beichman, C. A., Lisse, C. M., Tanner, A. M., et al. 2011, ApJ, 743, 85
Birnstiel, T., Dullemond, C. P., & Brauer, F. 2010, A&A, 513, A79
Bottke, W. F., & Norman, M. D. 2017, AREPS, 45, 619
Bouwman, J., Henning, T., Hillenbrand, L. A., et al. 2008, ApJ, 683, 479
Briceño, C., & Tokovinin, A. 2017, AJ, 154, 195
Bushouse, H., Eisenhamer, J., Dencheva, N., et al. 2023, JWST Calibration Pipeline, v1.12.5, Zenodo, doi:10.5281/zenodo.10022973
Cambioni, S., Asphaug, E., Emsenhuber, A., et al. 2019, ApJ, 875, 40
Cambioni, S., Weiss, B. P., Asphaug, E., et al. 2025, A&A, 696, A174
Carter, P. J., Leinhardt, Z. M., Elliott, T., Walter, M. J., & Stewart, S. T. 2015, ApJ, 813, 72
Carter, P. J., & Stewart, S. T. 2020, PSJ, 1, 45
Chambers, J. E. 2013, Icar, 224, 43
Charalambous, C., Cuello, N., & Petrovich, C. 2025, A&A, 696, A175
Chen, C. H., Li, A., Bohac, C., et al. 2007, ApJ, 666, 466
Chen, C. H., Mamajek, E. E., Bitner, M. A., et al. 2011, ApJ, 738, 122
Chen, C. H., Mittal, T., Kuchner, M., et al. 2014, ApJS, 211, 25
Chen, C. H., Sargent, B. A., Bohac, C., et al. 2006, ApJs, 166, 351
Chen, C. H., Su, K. Y. L., & Xu, S. 2020, NatAs, 4, 328
Chihara, H., Koike, C., Tsuchiyama, A., Tachibana, S., & Sakamoto, D. 2002, A&A, 391, 267
Contardo, G., & Hogg, D. W. 2024, AJ, 168, 157
Ćuk, M., Dones, L., & Nesvorný, D. 2016, ApJ, 820, 97
Dai, F., Goldberg, M., Batygin, K., et al. 2024, AJ, 168, 239
Davies, E. J., Carter, P. J., Root, S., et al. 2020, JGRE, 125, e06227
Davoisne, C., Djouadi, Z., Leroux, H., et al. 2006, A&A, 448, L1
de Vries, B. L., Skogby, H., Waters, L. B. F. M., & Min, M. 2018, Icar, 307, 400
Emsenhuber, A., Asphaug, E., Cambioni, S., et al. 2024, PSJ, 5, 59
Fabian, D., Jäger, C., Henning, T., Dorschner, J., & Mutschke, H. 2000, A&A, 364, 282
Fujiwara, H., Onaka, T., Yamashita, T., et al. 2012, ApJL, 749, L29
Gaidos, E., Jacobs, T., LaCourse, D., et al. 2019, MNRAS, 488, 4465
Genda, H., Kobayashi, H., & Kokubo, E. 2015, ApJ, 810, 136
Gentile Fusillo, N. P., Tremblay, P.-E., Gänsicke, B. T., et al. 2019, MNRAS, 482, 4570
Ghosh, T., Chatterjee, S., & Lombardi, J. C. 2024, AJ, 168, 238
Goldberg, M., & Batygin, K. 2022, AJ, 163, 201
Goldberg, M., & Petit, A. C. 2026, A&A, 707, A285
Gomes, R., Levison, H. F., Tsiganis, K., & Morbidelli, A. 2005, Natur, 435, 466
Gorlova, N., Balog, Z., Rieke, G. H., et al. 2007, ApJ, 670, 516
Hamer, J. H., & Schlaufman, K. C. 2024, AJ, 167, 55
Hansen, B. M. S. 2023, MNRAS, 520, 761
Harker, D. E., Wooden, D. H., Kelley, M. S. P., & Woodward, C. E. 2023, PSJ, 4, 242
Hartman, Z. D., & Lépine, S. 2020, ApJS, 247, 66
Hazen, R. M., Morrison, S. M., Prabhu, A., Walter, M. J., & Williams, J. R. 2023, AmMin, 108, 1620
Houck, J. R., Roellig, T. L., Van Cleve, J., et al. 2004, SPIE, 5487, 62
Hwang, H.-C., Ting, Y.-S., & Zakamska, N. L. 2022, MNRAS, 512, 3383
Izidoro, A., Ogihara, M., Raymond, S. N., et al. 2017, MNRAS, 470, 1750
Jackson, A. P., & Wyatt, M. C. 2012, MNRAS, 425, 657
Jang, H., Waters, R., Kaeufer, T., et al. 2024b, A&A, 691, A148
Jang, H., Waters, R., Kamp, I., & Dullemond, C. P. 2024a, A&A, 687, A275
Jensen, P. A., Shannon, M. J., Peeters, E., Sloan, G. C., & Stock, D. J. 2022, A&A, 665, A153
Johnson, B. C., Lisse, C. M., Chen, C. H., et al. 2012, ApJ, 761, 45
Johnson, B. C., & Melosh, H. J. 2012, Icar, 217, 416
Johnson, B. C., & Melosh, H. J. 2014, Icar, 228, 347
Johnson, B. C., Minton, D. A., Melosh, H. J., & Zuber, M. T. 2015, Natur, 517, 339
Juhász, A., Henning, T., Bouwman, J., et al. 2009, ApJ, 695, 1024
Juhász, A., Bouwman, J., Henning, T., et al. 2010, ApJ, 721, 431
Kaeufer, T., Min, M., Woitke, P., Kamp, I., & Arabhavi, A. M. 2024, A&A, 687, A209
Kemper, F., Vriend, W. J., & Tielens, A. G. G. M. 2004, ApJ, 609, 826
Kennedy, G. M., Ginski, C., Kenworthy, M. A., et al. 2020, MNRAS, 496, L75
Kennedy, G. M., Kenworthy, M. A., Pepper, J., et al. 2017, RSOS, 4, 160652
Kennedy, G. M., Murphy, S. J., Lisse, C. M., et al. 2014, MNRAS, 438, 3299
Kennedy, G. M., & Wyatt, M. C. 2013, MNRAS, 433, 2334
Kennedy, G. M., & Wyatt, M. C. 2014, MNRAS, 444, 3164
Kenworthy, M., Lock, S., Kennedy, G., et al. 2023, Natur, 622, 251
Kenyon, S. J., & Bromley, B. C. 2005, AJ, 130, 269
Kessler-Silacci, J., Augereau, J.-C., Dullemond, C. P., et al. 2006, ApJ, 639, 275
Koike, C., Chihara, H., Tsuchiyama, A., et al. 2003, A&A, 399, 1101
Koike, C., Noguchi, R., Chihara, H., et al. 2013, ApJ, 778, 60
Kraus, R. G., Stewart, S. T., Swift, D. C., et al. 2012, JGRE, 117, E09009
Kruegel, E. 2003, The Physics of Interstellar Dust (IOP Publishing)
Law, D. R., Argyriou, I., Gordon, K. D., et al. 2025, AJ, 169, 67
Lebouteiller, V., Barry, D. J., Spoon, H. W. W., et al. 2011, ApJS, 196, 8
Li, J., O'Connor, C. E., & Rasio, F. A. 2026, ApJL, 998, L5
Li, M. P., Zhao, G., & Li, A. 2007, MNRAS, 382, L26
Li, R., Chiang, E., Choksi, N., & Dai, F. 2025, AJ, 169, 323
Lieman-Sifry, J., Hughes, A. M., Carpenter, J. M., et al. 2016, ApJ, 828, 25
Lisse, C. M., Chen, C. H., Wyatt, M. C., et al. 2009, ApJ, 701, 2019
Lisse, C. M., Meng, H. Y. A., Sitko, M. L., et al. 2020, ApJ, 894, 116
Liu, B., Raymond, S. N., & Jacobson, S. A. 2022, Natur, 604, 643
Lovis, C., Mayor, M., Pepe, F., et al. 2006, Natur, 441, 305
Matrà, L., Marino, S., Wilner, D. J., et al. 2025, A&A, 693, A151
Melis, C., Olofsson, J., Song, I., et al. 2021, ApJ, 923, 90
Melis, C., Zuckerman, B., Rhee, J. H., & Song, I. 2010, ApJL, 717, L57
Meng, H. Y. A., Rieke, G. H., Su, K. Y. L., & Gáspár, A. 2017, ApJ, 836, 34
Meng, H. Y. A., Su, K. Y. L., Rieke, G. H., et al. 2014, Sci, 345, 1032
Meng, H. Y. A., Su, K. Y. L., Rieke, G. H., et al. 2015, ApJ, 805, 77
Min, M., Waters, L. B. F. M., de Koter, A., et al. 2007, A&A, 462, 667
Moór, A., Ábrahám, P., Kóspál, Á., et al. 2022, MNRAS, 516, 5684
Moór, A., Ábrahám, P., Su, K. Y. L., et al. 2024, MNRAS, 528, 4528
Moór, A., Ábrahám, P., Szabó, G., et al. 2021, ApJ, 910, 27
Morlok, A., Koike, C., Tomioka, N., Mann, I., & Tomeoka, K. 2010, Icar, 207, 45
Morlok, A., Lisse, C. M., Mason, A. B., Bullock, E. S., & Grady, M. M. 2014a, Icar, 231, 338
Morlok, A., Mason, A. B., Anand, M., et al. 2014b, Icar, 239, 1
Nesvorný, D., Vokrouhlický, D., Bottke, W. F., & Levison, H. F. 2018, NatAs, 2, 878
Ogihara, M., & Kunitomo, M. 2026, ApJ, 996, 91
Oliveira, I., Olofsson, J., Pontoppidan, K. M., et al. 2011, ApJ, 734, 51
Olofsson, J., Augereau, J.-C., van Dishoeck, E. F., et al. 2010, A&A, 520, A39
Olofsson, J., Augereau, J.-C., van Dishoeck, E. F., et al. 2009, A&A, 507, 327
Olofsson, J., Juhász, A., Henning, T., et al. 2012, A&A, 542, A90
Pascucci, I., & Sterzik, M. 2009, ApJ, 702, 724
Payne, M. J., Ford, E. B., Wyatt, M. C., & Booth, M. 2009, MNRAS, 393, 1219
Pontoppidan, K. M., Salyk, C., Banzatti, A., et al. 2024, ApJ, 963, 158
Poon, S. T. S., Nelson, R. P., Jacobson, S. A., & Morbidelli, A. 2020, MNRAS, 491, 5595
Przygodda, F., van Boekel, R., Àbrahàm, P., et al. 2003, A&A, 412, L43
Quarles, B., & Kaib, N. 2019, AJ, 157, 67

Quintana, E. V., Barclay, T., Borucki, W. J., Rowe, J. F., & Chambers, J. E. 2016, ApJ, 821, 126
Raymond, S. N., Armitage, P. J., & Gorelick, N. 2010, ApJ, 711, 772
Rhee, J. H., Song, I., & Zuckerman, B. 2008, ApJ, 675, 777
Rieke, G. H., Su, K. Y. L., Melis, C., & Gáspár, A. 2021, ApJ, 918, 71
Rodriguez, D. R., Marois, C., Zuckerman, B., Macintosh, B., & Melis, C. 2012, ApJ, 748, 30
Roumeliotis, Z., Matrà, L., Kennedy, G. M., et al. 2026, A&A, 706, A4
Samland, M., Henning, T., Caratti o Garatti, A., et al. 2025, ApJ, 989, 132
Sargent, B., Forrest, W. J., D'Alessio, P., et al. 2006, ApJ, 645, 395
Sargent, B. A., Forrest, W. J., Tayrien, C., et al. 2009a, ApJ, 690, 1193
Sargent, B. A., Forrest, W. J., Tayrien, C., et al. 2009b, ApJS, 182, 477
Schneider, A., Song, I., Melis, C., et al. 2013, ApJ, 777, 78
Shah, S., Marshall, J. P., del Burgo, C., et al. 2026, MNRAS, 546, staf2251
Smit, J. 1999, AREPS, 27, 75
Stewart, S. T., & Leinhardt, Z. M. 2012, ApJL, 751, 32
Strom, R. G., Malhotra, R., Ito, T., Yoshida, F., & Kring, D. A. 2005, Sci, 309, 1847
Su, K. Y. L., Jackson, A. P., Gáspár, A., et al. 2019, AJ, 157, 202
Su, K. Y. L., Kennedy, G. M., Rieke, G. H., et al. 2023, ApJ, 959, 43
Su, K. Y. L., Kennedy, G. M., Schlawin, E., Jackson, A. P., & Rieke, G. H. 2022, ApJ, 927, 135
Su, K. Y. L., Moór, A., Xie, C., et al. 2025, ApJL, 988, L2
Su, K. Y. L., Rieke, G. H., Melis, C., et al. 2020, ApJ, 898, 21
Thompson, M. A., Weinberger, A. J., Keller, L. D., Arnold, J. A., & Stark, C. C. 2019, ApJ, 875, 45
Thompson, S. P., Herlihy, A., Murray, C. A., et al. 2019, A&A, 624, A136
Varga, J., Henning, T., Waters, L. B. F. M., et al. 2026, A&A, 711, A125
Verbiscer, A. J., Skrutskie, M. F., & Hamilton, D. P. 2009, Natur, 461, 1098
Volk, K., & Gladman, B. 2015, ApJL, 806, L26
Voshchinnikov, N. V., & Henning, T. 2008, A&A, 483, L9
Watson, D. M., Leisenring, J. M., Furlan, E., et al. 2009, ApJS, 180, 84
Watt, L., Leinhardt, Z. M., & Carter, P. J. 2024, MNRAS, 527, 7749
Weinberger, A. J., Becklin, E. E., Song, I., & Zuckerman, B. 2011, ApJ, 726, 72
Wong, K. H., & Lee, M. H. 2024, AJ, 167, 112
Wooden, D. H. 2002, EM&P, 89, 247
Worthen, K., Chen, C. H., Hughes, A. M., et al. 2026, ApJ, 997, 94
Wright, G. S., Wright, D., Goodson, G. B., et al. 2015, PASP, 127, 595
Wu, Y., Malhotra, R., & Lithwick, Y. 2024, ApJ, 971, 5
Wyatt, M. C. 2008, A&A, 46, 339
Wyatt, M. C., Smith, R., Greaves, J. S., et al. 2007, ApJ, 658, 569
Zakamska, N. L., Adamane Pallathadka, G., Bizyaev, D., et al. 2026, AJ, 171, 95
Zuckerman, B. 2015, ApJ, 798, 86